

ARMY RESEARCH LABORATORY



An Investigation of the Ballistic Performance for an Electromagnetic Gun-Launched Projectile

by Alexander E. Zielinski, Paul Weinacht,
David W. Webb, and Keith P. Soencksen

ARL-TR-1361

June 1997

19970623 123

Approved for public release; distribution is unlimited.

DTIC QUALITY INSPECTED 4

The findings in this report are not to be construed as an official Department of the Army position unless so designated by other authorized documents.

Citation of manufacturer's or trade names does not constitute an official endorsement or approval of the use thereof.

Destroy this report when it is no longer need. Do not return it to the originator.

Army Research Laboratory

Aberdeen Proving Ground, MD 21005-5066

ARL-TR-1361**June 1997**

An Investigation of the Ballistic Performance for an Electromagnetic Gun-Launched Projectile

**Alexander E. Zielinski, Paul Weinacht, David W. Webb,
Keith P. Soencksen**

Weapons and Materials Research Directorate, ARL

Abstract

The Cannon-Caliber Electromagnetic Gun (CCEMG) Program is a major effort toward proving the viability of electromagnetic (EM) weapons for future use by the armed services. Crucial to the success of the program are the operational characteristics of the launcher and the integrated launch package (ILP), which consists of an armature/sabot and a subprojectile. To date, 39 shots have been fired at the U.S. Army Research Laboratory (ARL) using a 1.6-MJ capacitor bank and CCEMG Launcher IIa. Free-flight aerodynamic data indicated that the subprojectile has adequate in-flight stability. An analysis of the transitional ballistic process has been performed to quantify the contributors to the total launch disturbance. The jump component dispersion and target impact dispersion are larger in the vertical direction than in the horizontal direction. In the vertical direction, the center of gravity and aerodynamic jump contributions are dominant and roughly equal. In the horizontal direction, the sabot discard is the dominant jump component. Round-to-round dispersion was computed over a wide range of launch velocities based on downrange impact locations. Impact data on armor were limited, but nonetheless indicated that the round is capable of meeting the CCEMG system requirements. The results presented here represent the first known experimental assessment of these parameters obtained from EM railgun firings.

Acknowledgments

Funding for this effort was provided by the Close Combat Armaments Center (CCAC) of the U.S. Army Armament Research, Development and Engineering Center (ARDEC), the U.S. Marine Corps (USMC), and the U.S. Army Research Laboratory (ARL). Significant contributions in support of the experimental results were made by Mr. Ken Paxton, Mr. Steve Niles, and Mr. Barry Hudler. The assistance of Mr. Timothy Farrand in the assessment of the terminal ballistic data is greatly appreciated. We also thank Dr. Peter Plostins and Dr. Mark Bundy for careful review of this report and for helpful discussions.

INTENTIONALLY LEFT BLANK.

TABLE OF CONTENTS

	<u>Page</u>
Acknowledgments	iii
List of Figures	vii
List of Tables	ix
1. Introduction	1
2. Experiment	4
3. Free-Flight Data and Analysis	16
3.1 Reduction of the Free-Flight Angular Motion	17
3.2 Aerodynamic Predictions	19
3.3 Aerodynamic Performance of the Subprojectile	20
3.4 Reduction of the Swerving Motion	24
4. Jump	24
4.1 Jump Description	24
4.2 Jump Component Determination	25
4.3 Bias and Dispersion of the Jump Components	30
5. Target Impact Dispersion and Accuracy	37
6. Terminal Performance	40
7. Summary	42
8. References	45
Distribution List	47
Report Documentation Page	51

INTENTIONALLY LEFT BLANK.

List of Figures

<u>Figure</u>	<u>Page</u>
1. Schematic illustration of a simple railgun	1
2. CCEMG launcher cross section	3
3. Photograph of recently tested ILP	4
4. Orthogonal x-ray photographs of ILP at muzzle exit for shot 39	5
5. Photograph of first-generation ILP	11
6. Schematic illustration of the six-fin fluted-flare stabilized subprojectile	12
7. Schematic illustration of the four-fin swept-delta stabilized subprojectile	12
8. Current pulse applied to the launcher and switch current, shot 38	13
9. Resultant ILP current, shot 38	14
10. Measured projectile current, shot 39	15
11. Computed ILP acceleration, shot 39	15
12. Fit of the measured angular motion from shot 24, α - dashed line, β - solid line	18
13. Pitching moment coefficient, C_{m_α} , as a function of velocity	21
14. Waterfall plot radar indicating velocity history of subprojectile and armature/sabot	21
15. Coefficient of drag, C_D , as a function of velocity	22
16. Normal force coefficient, C_{N_α} , as a function of velocity	23
17. Pitch-damping coefficient, $C_{m_q} + C_{m_{\dot{\alpha}}}$, as a function of velocity	23
18. Schematic depiction of jump components from aim point to target impact	25
19. Multistation, orthogonal flash x-ray images from shot 26 (launch velocity = 1,087 m/s)	26
20. Jump vector diagram for shot 26	29
21. Displacement from bore centerline (horizontal plane)	30
22. Displacement from bore centerline (vertical plane)	31
23. Jump component dispersions (CG, AJ, SD) for shots 20, 24-26, and 27	32
24. Percentage comparison of jump component dispersions (CG, AJ, SD) for shots 20, 24-26, and 27	33

25.	Dispersion for AJ and LD jump components as a function of average launch velocity	34
26.	Fitted free-flight (solid line) and muzzle (dashed line) yaw amplitude for shot 16	35
27.	Muzzle and maximum free-flight angular rates for shots 25 and 26	36
28.	Separation distance between the subprojectile and the front of armature . . .	36
29.	Target impact dispersion in azimuth and elevation (confidence intervals are indicated at 1,850 m/s)	38
30.	Vertical target impact locations with and without honing between shots, 30–35 m targets	39
31.	Horizontal target impact locations with and without honing between shots, 30–35-m targets	40
32.	Front view of armor target and five subprojectile impacts	41
33.	Terminal performance of the ILP subprojectile as a function of effective range	41

List of Tables

<u>Table</u>		<u>Page</u>
1.	CCEMG SOW Requirements	2
2.	Summary of Component Characterization Shots	6
3.	Summary of Armature Development Shots With Six-Fin Fluted-Flare Subprojectile	7
4.	Summary of Launch Dynamics Shots With Four-Fin Swept-Delta Afterbody	8
5.	Summary of Pseudo-Multishot Test	9
6.	Summary of High-Current Shots	10
7.	Physical Properties of Subprojectile	19

INTENTIONALLY LEFT BLANK.

1. Introduction

The Cannon-Caliber Electromagnetic Gun (CCEMG) Program is jointly sponsored by the U.S. Army Armament Research, Development, and Engineering Center and the U.S. Marine Corps. A primary goal of the CCEMG program is the successful demonstration of a multishot weapon based on electromagnetic (EM) gun technology. The University of Texas, Center for Electromechanics (UT-CEM) is tasked with the pulsed power supply (PPS), launcher, and armature development,^{1, 2, 3} and Kaman Science Corporation is tasked with the development of the Integrated Launch Package (ILP).⁴ The U.S. Army Research Laboratory (ARL) was responsible for assessing single-shot performance of the launcher and ILP. This report documents the results of the single-shot testing performed at the EM Facility at the ARL Transonic Experimental Facility (TEF), Aberdeen Proving Ground (APG), MD.

The essential features of a simple electromagnetic launcher (EML) are illustrated in Figure 1. A current is applied to a parallel pair of conducting rails. The rails, with a parallel pair of insulators orthogonal to the rail pair, form the bore cross section. A conductor, which is free to slide between the rail pair, completes the circuit and also carries the same current. The moving conducting element is called the armature. The cross product between the armature current I and the magnetic induction field B produced in the bore results in a force tending to expand the current-carrying loop that leads to the acceleration of the armature. The force accelerating the armature can be found from the gradient of the magnetic energy E_m associated with the current-carrying loop.

$$F = -\nabla E_m \quad (1)$$

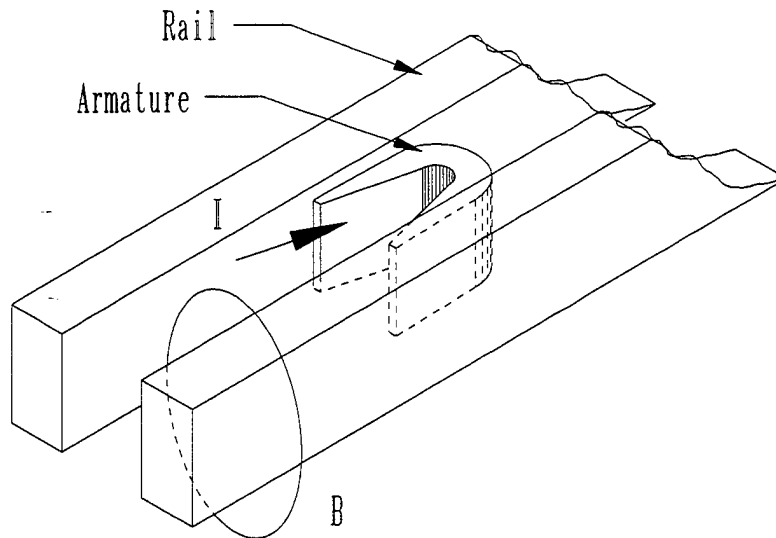


Figure 1. Schematic illustration of a simple railgun.

The gradient of the magnetic energy can also be written in terms of the current I and the gradient of the inductance in the direction of armature acceleration.

$$F = \frac{1}{2} L' I^2 \quad (2)$$

The inductance gradient L' can be computed from the conductor and bore geometries with sufficient accuracy for most configurations of interest.⁵ In the CCEMG launcher, an extra conductor located behind each bore rail is connected electrically in series with the rails. The extra conductors form a loop (i.e., turn) traversing the length of the launcher and augmenting the magnetic field in the bore. The result is an increase in the inductance gradient. This beneficial increase, however, is diminished by the additional resistance of the augmenting turn. Nonetheless, the CCEMG launcher has managed these effects through efficient conductor topology, bore geometry, and pulsed-power considerations to produce highest railgun efficiency to date.²

Early in the design process, an optimization code⁶ was developed (EXCALIBER) to identify ideal EML system parameters such as the launcher and ILP geometry and the power supply configuration. This code is based on a "breach-to-target" approach⁷ using terminal performance at range and PPS mass and volume to determine viable systems. The optimization, using CCEMG statement of work (SOW) parameters (Table 1), resulted in a rectangular bore cross section. The CCEMG armature serves two functions; first, it carries the accelerating current and, second, it distributes the accelerating force to the subprojectile along a large portion of its length. As such, the armature must be discarded after launch much like a conventional sabot. This dual-purpose armature/sabot makes contact with the rail at two distinct places (tandem contact), is all aluminum, and has a rectangular cross section. The launch package mass computed from EXCALIBER is 180 g: 90-g armature and 90-g subprojectile.

Table 1. CCEMG SOW Requirements.

	SOW Requirement
Armor Penetration, at 56° obliquity	131 mm RHA @1.5 km 66 mm RHA @3 km
Caliber	20 to 40 mm
Firing Rate	300 to 400 rounds per minute
Salvo Size	5 to 7 rounds
Time Between Salvos	2-2.5 s
Probability of Hit	0.9
System Weight	5,000-lb maximum
Weapon Platform	Compatible with Amphibious Assault Vehicle

The "series-augmented" launcher is 2.25 m long. Only the first 1.85 m of the gun is augmented. The railgun bore geometry is rectangular - 17.5 mm \times 39 mm (Figure 2). The CCEMG railgun incorporates several unique features: ceramic sidewalls, internal preloading, and chromium copper rails.

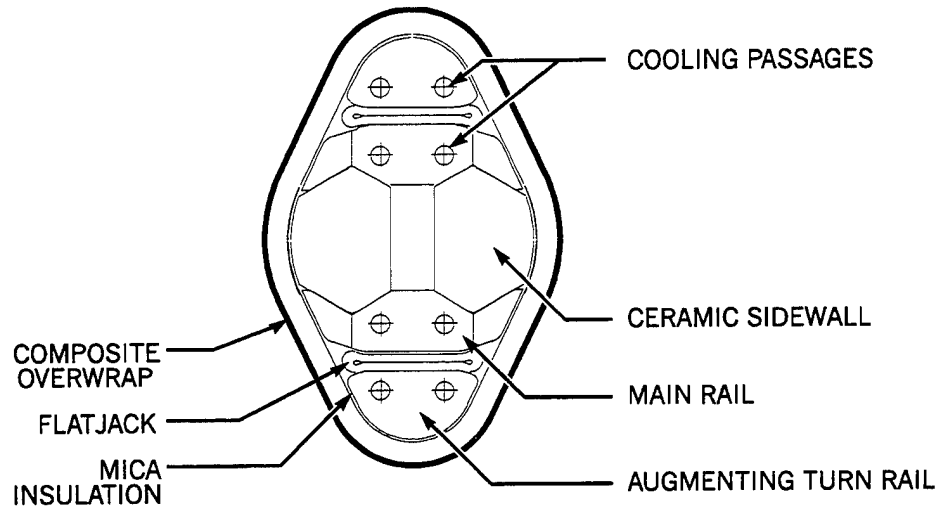


Figure 2. CCEMG launcher cross section.

Directional preloading mechanisms called "flatjacks" located between the main and augmenting rails (Figure 2) are utilized to counter EM loading and maintain a compressive state in the alumina ceramic sidewalls (AD-96 alumina). The success of the launcher design depends heavily on the flatjacks' ability to apply pressure to the main rails so that the ceramic sidewalls remain in compression throughout the discharge. This results in an extremely stiff launcher design. The preloaded sidewalls are reacted against a filament-wound composite overwrap composed of 82% 90° graphite fibers and 18% 0° fiberglass. The overwrap reacts the preload plus a fraction of the EM loading and provides stiffness to the launcher in the axial direction. These features give the launcher a peak bore growth of 0.2% at full EM loading and an overall weight of 273 kg.

Chromium copper (C18200) was chosen as the rail material because of its strength (310-Mpa yield), conductivity (82% International Annealed Copper Standard [IACS]), relatively low cost, and its dimensional stability. To attain the launcher's high efficiency, the main rails are slit (1.6 mm wide on 3.2-mm centers) transverse to the gun's axis to the midpoint of the ceramic sidewall. This region of the main rail is required for structural purposes, but, left solid, is detrimental to magnetic performance.

To meet the penetration at range requirement, the ILP is designed to operate at a launch velocity of 1,850 m/s. This results in a peak axial acceleration of 2.06×10^6 m/s² (210,000 g's). The armature forms a two-piece sabot that conforms to the rectangular bore of the gun and encases the subprojectile. A longitudinal cut through the armature in the

vertical direction (along the major axis of the cross section) allows the armature/sabot to separate from the subprojectile after launch. A photograph of a recently tested ILP is shown in Figure 3.

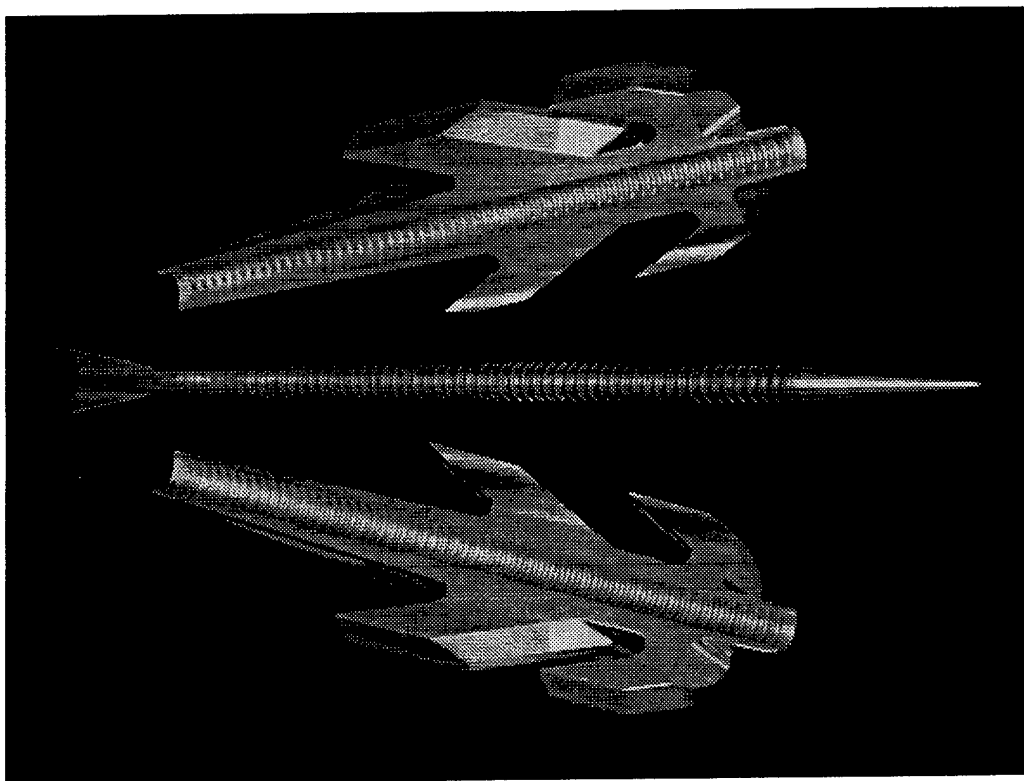


Figure 3. Photograph of recently tested ILP.

Testing took place at the EM Facility, TEF, APG, MD. The facility consists of a 1.6-MJ, capacitor-based PPS with a 222-m free-flight range.⁸ The PPS comprises eight banks, each with the flexibility to be charged to a different initial voltage, as well as to be triggered independently in time. Each bank is nominally 200 kJ at a rated maximum charge voltage of 10 kV. Each bank is connected to a common bus through a D-size ignitron and a nominal 10- μ H inductor. Stacks of diodes prevent voltage reversal across the capacitors. During the last phase of testing, the power supply was capable of producing a peak admittance of 84 kA/kV. The rise to peak current was sinusoidal and occurred at 0.46 ms. Shortly after reaching its peak, the current exhibits an exponential decay with a 3-ms time constant.

2. Experiment

The primary objective of the experimental test program was to verify the single-shot launcher and ILP performance in support of achieving the CCEMG system requirements.⁹ The tests were performed over a period of one year. During the course of the single-shot tests, the ILP was subject to increasing levels of acceleration to verify its structural integrity. Testing was planned such that an abundance of relevant data could be obtained early in the

program without placing the hardware at unnecessary risk. A developmental approach to testing allowed the EM Facility, launcher, and ILP to be improved during the various phases of testing. As a result, the ILP was eventually tested at 86% of its peak axial structural rating (96% of full design velocity) and verified with x-ray images (shown in Figure 4) and successful target impact at range.

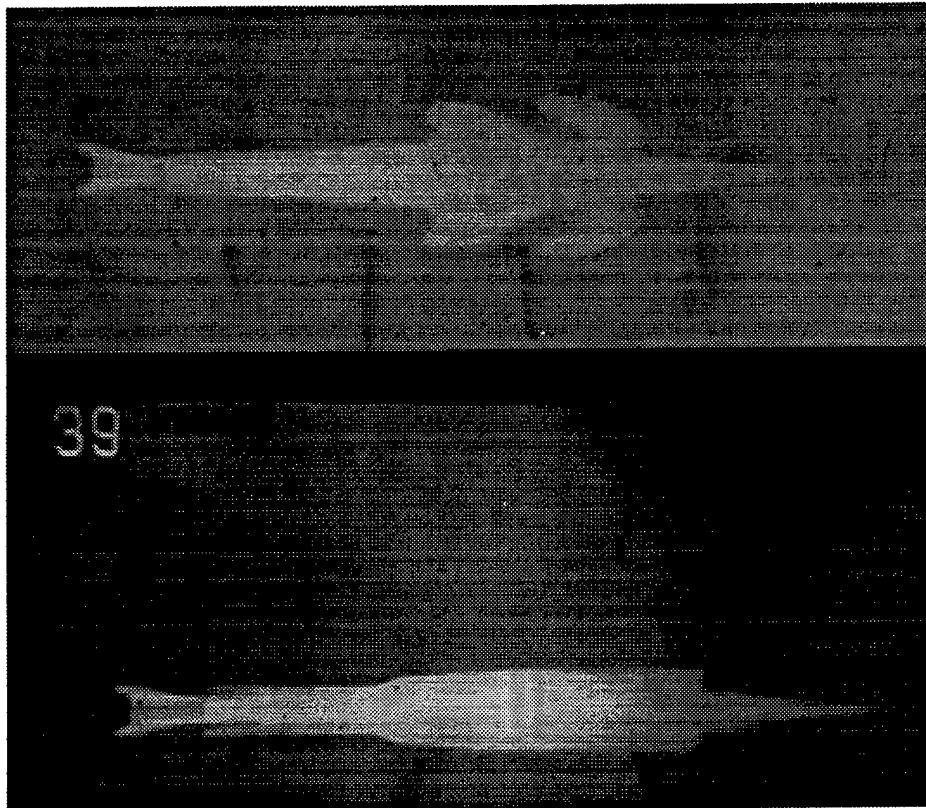


Figure 4. Orthogonal x-ray photographs of ILP at muzzle exit for shot 39.

The testing was grouped into several phases; component characterization (shots 1-9), armature development (shots 10-16), launch dynamics (shots 17-27), psuedo-multishot (shots 28-32) and peak performance (shots 33-39). Tabular summaries of each of the five phases of testing are presented in Tables 2-6. These tables present data characterizing the launcher and launch package performance for each shot. Column 1 identifies the ARL shot number. Columns 2 through 4 present electrical performance data taken during each shot. Parameters pertaining to the launch package such as ILP identification, mass, exit velocity and the force required to insert the ILP into the launcher are listed in the next four columns. Finally, in the last column, significant comments and observations pertaining to each shot are listed.

Table 2. Summary of Component Characterization Shots.

Shot Number	Electrical Parameters			Launch Package Information				Comments and Observations
	V_{charge} (kV)	I_{pk} (kA)	I_{exit} (kA)	Type	Mass (g)	Velocity (m/s)	F_{insert} (kN)	
1	5.0	372	156	1 piece Al slug	98	971	3.99	Power supply checkout.
2	6.0	434	187	1 piece Al slug	98	1205	4.38	Power supply checkout.
3	6.0	430	179	1 piece Al slug	98	1269	3.39	Power supply checkout.
4	7.0	502	219	1 piece Al slug	135	1101	7.77	Instrumentation checkout.
5	8.0	571	266	1 piece Al slug	136	1538	6.98	Instrumentation checkout.
6	8.0	577	274	1 piece Al slug	98	1785	2.24	Instrumentation checkout. Postshot in-bore video.
7	8.5	609	294	1 piece Al slug	98	1886	2.79	Instrumentation checkout. Postshot in-bore video. Black and white Fastex.
8	8.0	588	264	1 piece Al slug	136	1515	6.77	Instrumentation checkout. Color Fastex.
9	8.5	619	276	3 piece Al/Wa slug	182	1333	4.58	Muzzle x-rays. Postshot bore centerline measured.

Table 3. Summary of Armature Development Shots With Six-Fin Fluted-Flare Subprojectile.

Shot Number	Electrical Parameters			Launch Package Information			Comments and Observations
	V_{charge} (kV)	I_{pk} (kA)	I_{exit} (kA)	Type	Mass (g)	Velocity (m/s)	F_{insert} (kN)
10	5.0	368	142	First generation ILP	173	735	7.97
11	5.0	333	125	Design B ILP	177	633	6.38
12	7.0	456	187	First generation ILP	174	1000	4.78
13	7.0	459	192	First generation ILP	172	980	7.38
14	9.0	586	263	First generation ILP	174	1370	5.98
15	7.0	460	192	First generation ILP	173	980	7.57
16	9.2	667	288	First generation ILP	178	1492	7.57

Table 4. Summary of Launch Dynamics Shots With Four-Fin Swept-Delta Afterbody.

Shot Number	Electrical Parameters			Launch Package Information			Comments and Observations
	V_{charge} (kV)	I_{pk} (kA)	I_{exit} (kA)	Serial Number	Mass (g)	Velocity (m/s)	F_{insert} (kN)
17	7.5	547	239	9008/01	179	1139	4.48
18	7.5	545	238	9008/02	179	1140	4.19
19	7.5	405	178	9008/03	179	842	5.48
20	7.5	407	178	9008/05	179	826	5.48
21	7.5	-	-	9008/04	178	1190	5.48
22	7.5	508	224	9008/06	178	1087	5.48
23	7.5	550	235	9008/07	178	1190	5.48
24	7.5	409	172	9008/08	179	848	3.99
25	7.5	509	220	9008/10	177	1075	5.48
26	7.5	510	218	9008/09	178	1087	5.48
27	7.5	409	177	9008/00-11	178	847	5.48

Table 5. Summary of Pseudo-Multishot Test.

Shot Number	Electrical Parameters			Launch Package Information			Comments and Observations
	V_{charge} (kV)	I_{pk} (kA)	I_{exit} (kA)	Serial Number	Mass (g)	Velocity (m/s)	
28	6.4	548	248	9008/01-01	178	1176	Orthogonal smear camera and Weibel radar. 60° high-hard armor (HHA) target at 222 m.
29	6.4	537	244	9008/01-02	178	1176	Two station orthogonal x-rays.
30	6.4	547	244	9008/01-04	179	1190	Penetrated HHA target.
31	6.4	500	217	9008/01-03	179	1064	Penetrated HHA target.
32	6.4	505	231	9008/01-05	179	1053	Penetrated HHA target.
							Bore dimension in rail plane measured postshot.

Table 6. Summary of High-Current Shots.

Shot Number	Electrical Parameters			Launch Package Information			Comments and Observations	
	V_{charge} (kV)	I_{pk} (kA)	I_{exit} (kA)	Serial Number	Mass (g)	Velocity (m/s)		F_{insert} (kN)
33	6.4	559	150	9008/01-06	179	1191	5.73	Three station orthogonal x-rays.
34	7.4	639	132	9008/01-10	180	1354	5.58	Poor sabot discard.
35	8.5	660	125	9008/01-09	180	1452	5.58	Perforated oblique HHA target and penetrated steel backing plate.
36	7.7	645	114	9008/01-16	179	1428	5.58	First shot after upgrade to 1.6-MJ power supply. Round hit instrumentation mount.
37	7.8	666	146	9008/01-07	180	1492	5.58	Orthogonal smear.
38	8.6	716	134	9008/01-11	180	1639	5.58	Perforated HHA and steel backing plate. Orthogonal and side view downrange smear cameras.
39	9.1	766	384	9008/01-14	180	1785	5.58	Verified ILP structural integrity. Radar data.

The component characterization phase focused on an initial assessment of the launcher and power supply operation and performance. These shots utilized slugs instead of the ILP. Portions of the ARL tests duplicated the test results from the 11 shots made by UT-CEM prior to the delivery of the launcher to ARL.¹⁰ One of the shots during the component characterization phase exceeded the CCEMG design velocity with an armature contact design similar to the one used in the current ILP. The bore surface was surveyed with a bore scope, and no evidence of rail gouging was seen. However, recent analysis of the decommissioned launcher², as well as analysis of the muzzle voltage data, indicates that nearly all the armatures did not maintain a solid contact with the rail surface. It is likely that the presence of a plasma interface between the rail surface and armature tended to reduce or obscure the effects of gouging.

In the armature development phase, tests were performed with a first-generation ILP design. The ILP shown in Figure 5 consisted of a six-fin fluted-flare subprojectile, shown schematically in Figure 6, and a baseline armature design. Test results identified improvements to minimize sabot discard disturbances. Testing was limited to a range of 50 m. Design changes to the subprojectile and armature were implemented after shot 16.

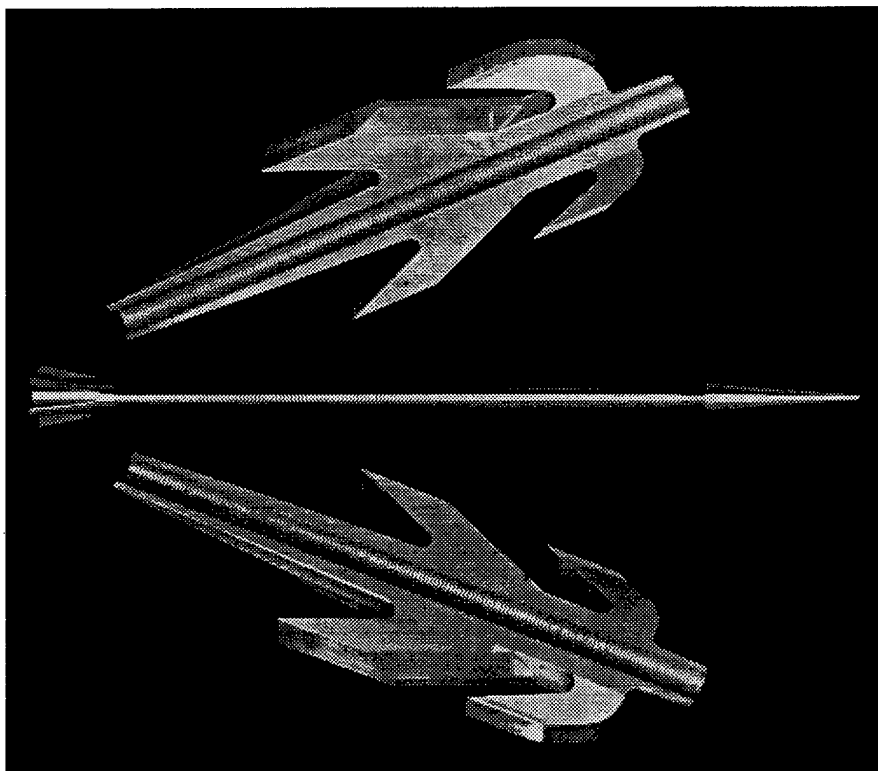


Figure 5. Photograph of first-generation ILP.

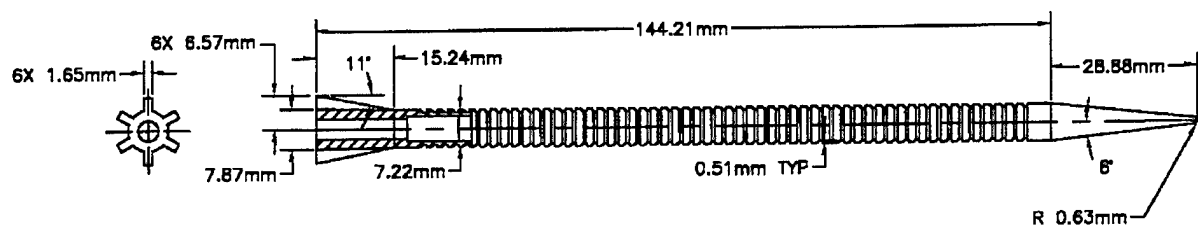


Figure 6. Schematic illustration of the six-fin fluted-flare stabilized subprojectile.

In the launch dynamics phase of testing, the subprojectile used a four-fin afterbody that exhibited improved aerodynamic stability. A schematic of the four-fin subprojectile is shown in Figure 7. In addition, the armature was modified to incorporate features that would enhance the aerodynamic separation of the sabot/armature halves following muzzle exit. These included the addition of an air scoop in the front of each armature half, steel pins to allow the armature to pivot off the rear of the subprojectile, and less mechanical interference between the rod and armature halves. The target impact plate was placed at the full flat-fire trajectory of 222 m. These tests were necessary to gain an understanding of the dispersion and to assess the components contributing to dispersion in order to implement any additional design modifications.

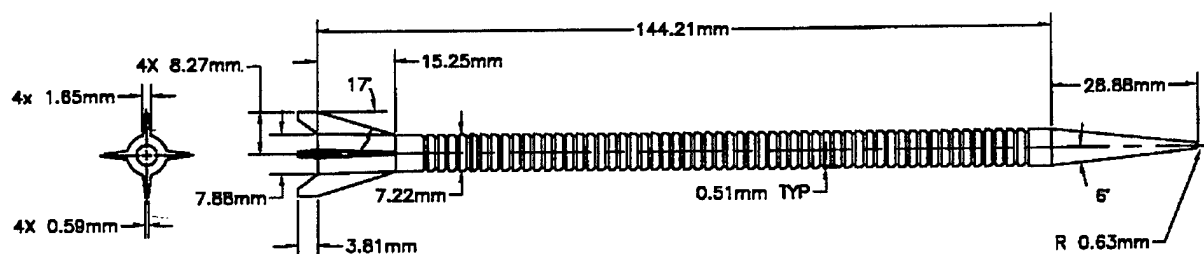


Figure 7. Schematic illustration of the four-fin swept-delta stabilized subprojectile.

CCEMG is a multishot demonstrator. The tests reported here are single-shot. However, as a precursor to eventual multishot operation of the CCEMG, five consecutive shots (shots 28–32) were performed at previously demonstrated launch velocities without bore maintenance between shots. The power supply was upgraded just prior to this phase to its present capability of 1.6 MJ of stored energy at 10 kV.

In the final phase of testing, the launcher and ILP were subjected to maximum stress levels. This is simply accomplished by increasing the initial capacitor charge voltage and resultant peak current delivered to the launcher. In order to realize peak performance with a capacitor-based power supply, an explosively activated closing switch was connected across the rails near the muzzle end of the launcher and closed prior to projectile exit. The switch was incorporated to reduce the exponentially decaying current and arc at projectile exit, which can lead to excessive wear and fatigue at the muzzle. Previously demonstrated currents at projectile exit greater than 250 kA were suspected to cause severe structural deformation at the muzzle. The current pulse applied to the launcher and the switch current from shot 38 are shown in Figure 8. The resultant ILP current is the difference between the launcher current and the switch current and is shown in Figure 9.

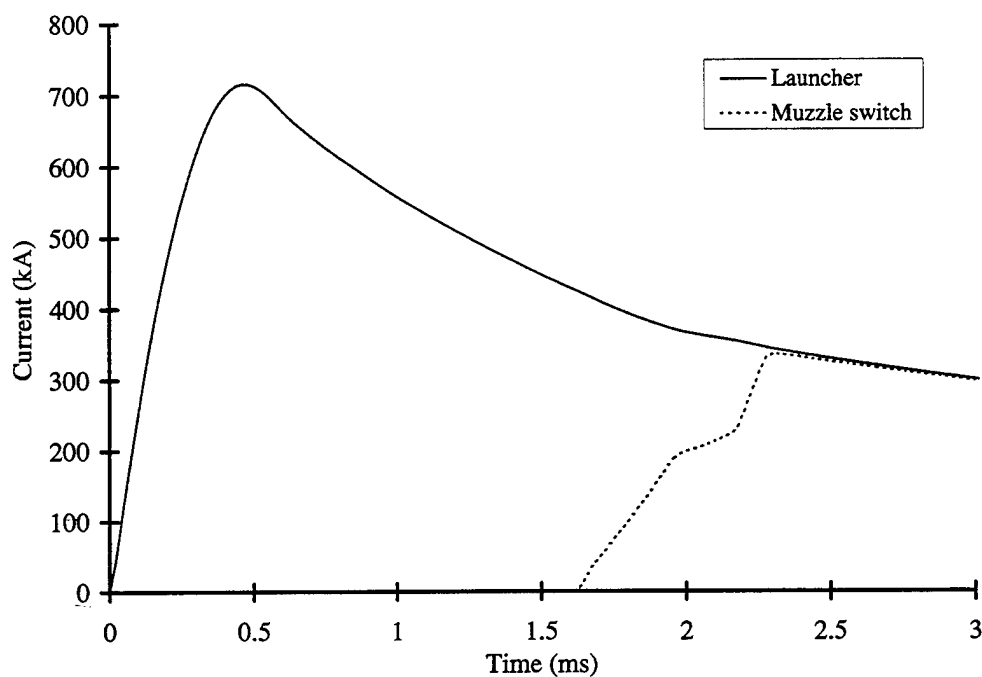


Figure 8. Current pulse applied to the launcher and switch current, shot 38.

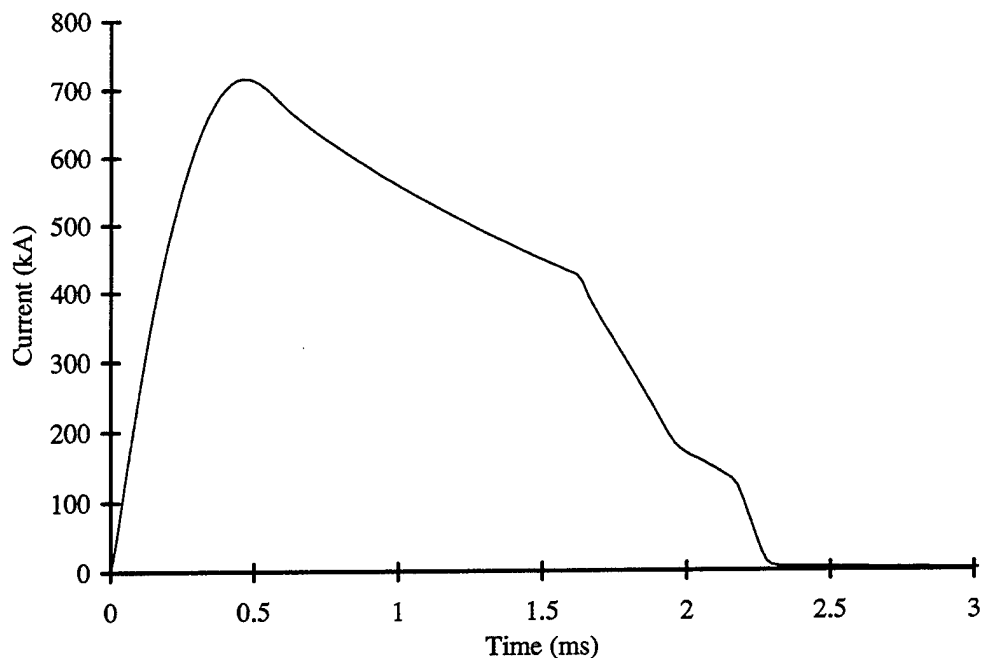


Figure 9. Resultant ILP current, shot 38.

The highest launcher current was 766 kA and occurred on shot 39. On this shot, the current flowing in the armature at projectile exit was also the highest at 384 kA because the muzzle switch was not placed in the “armed” position prior to the shot and did not function near shot exit. It is noteworthy that during the shot, the detonators (RP-80) used to trigger the muzzle switch were not activated unintentionally by the strong electric and magnetic fields associated with the launcher, even though they are located with 0.1 m of the launcher. While further studies on the effects of electric gun magnetic and electric fields on high explosives still need to be performed, this limited evidence seems to suggest the potential for launching high-explosive projectiles from electric guns. During the shot, the trigger system also did not generate spurious signals that would falsely trigger the switch. Nonetheless, the round successfully flew and impacted the target downrange. Measured launcher current and computed ILP acceleration are plotted in Figures 10 and 11, respectively. The PPS was charged to an initial voltage of 9.1 kV, yielding a transfer admittance of 84 kA/kV. The current rise to peak occurred at 0.46 ms, and the projectile exited the launcher at 2.04 ms with a velocity of 1,785 m/s. Thereafter, the slope of the current changes because of the high-impedance arc at the muzzle. Other electrical data acquired during the shot include the breech, launcher, and muzzle voltages. The electrical performance of the launcher is presented elsewhere.²

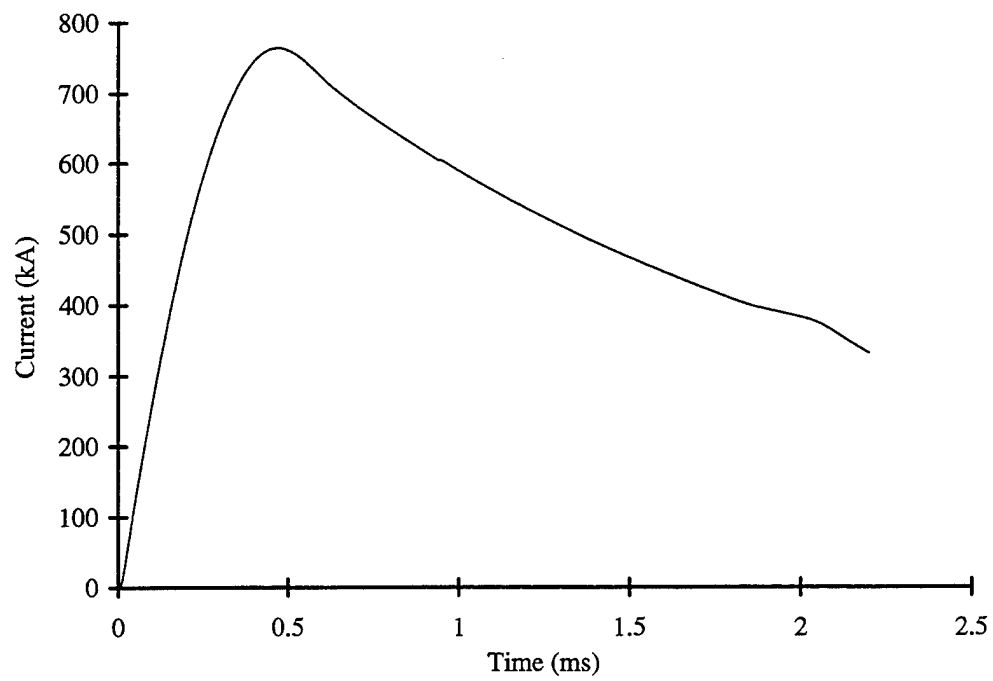


Figure 10. Measured projectile current, shot 39.

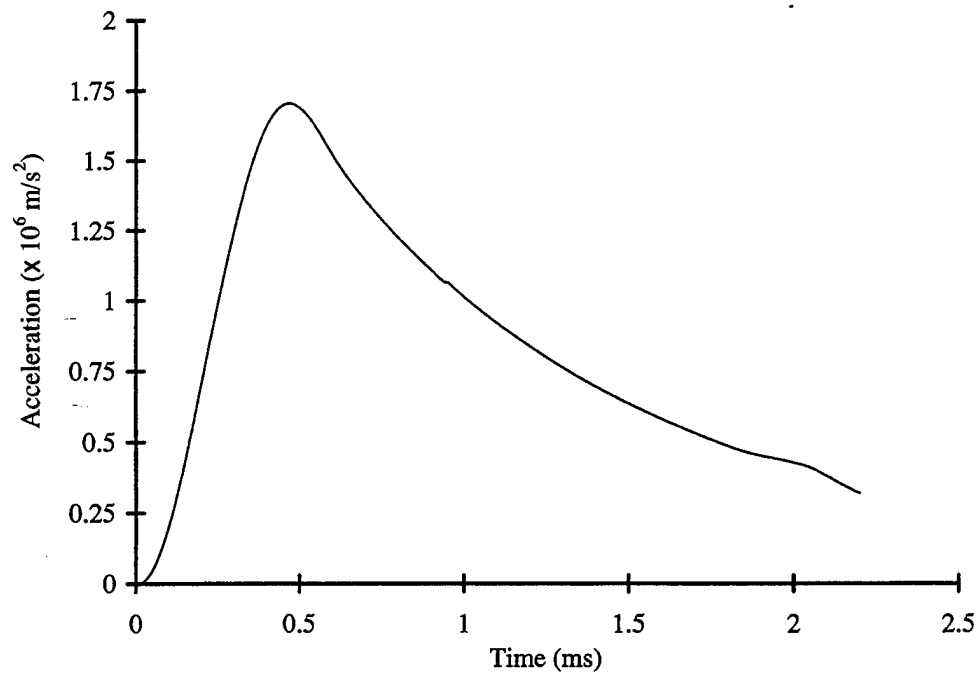


Figure 11. Computed ILP acceleration, shot 39.

A number of different measurement techniques were used to assess muzzle velocity. Measurements based on the time rate of change of the armature's in-bore induction field (dB/dt) were recorded for all the shots. Smear camera, flash x-ray, radar, and break screen techniques were also employed, though none of these measurements were available for all the shots. The velocity measurements obtained from the dB/dt signals were within 4% of values from the other techniques. All velocities reported in this paper are inferred from dB/dt signals.

To evaluate launch dynamics, an aim point and intended line of flight were established a few meters downrange of the muzzle by using a boresight and mount. A pulley was securely fastened 4 m downrange and aligned with the boresight crosshairs. A cable was attached at the breech, pulled through the launcher, and suspended over the pulley using a 50-kg weight to tension the cable. The cable, for indicating line of flight, and beads, for referencing the subprojectile center of gravity (c.g.), were superimposed upon each x-ray.¹¹

Yaw cards (cardboard targets) were consistently used to assess the free-flight aerodynamics of the projectile. As many as 15 yaw cards were placed at measured intervals along the trajectory and boresighted. After each shot, the horizontal and vertical displacements of the flight body from the original aim point, as well as the angle of attack (AoA) produced by the pitching and yawing motion, were measured from the impact on the yaw card. In the absence of x-rays, yaw cards were often used to qualitatively evaluate the sabot discard.

Radar was used after shot 27 to assess the subprojectile velocity degradation over the flight range. The radar unit was placed 11 m downrange. Triggering was accomplished by aiming a light sensitive sensor at the muzzle, 13 m from the line of flight.

A high-speed camera was used to obtain a down-bore view of the armature discard. Many problems were experienced in trying to resolve the ILP image particularly in the presence of a muzzle arc. One attempt was successful when a large thick sheet of paper was placed across the front of the muzzle. The paper tended to block the backlighting provided by the plasma arc. Smear cameras were also routinely used to assess the sabot discard. The most common configuration was where the camera was set up to take an orthogonal view. The camera was placed 4.6 m downrange, perpendicular to the line of flight. A mirror was placed at 45° opposite the camera. Number 2 flash bulbs were used to illuminate the ILP.

3. Free-Flight Data and Analysis

The free-flight performance of the subprojectile was assessed by measuring the angular motion and the displacement of the center of gravity using a series of yaw cards placed along the flight path of the projectile. The measurement of the free-flight dynamic response of the subprojectile allows a quantitative assessment of the aerodynamic performance of the subprojectile and the launch and sabot disturbances that drive the free-flight motion.

3.1 Reduction of the Free-Flight Angular Motion

The measured free-flight yawing (angular) motion was fit using closed-form solutions of the equations of motion for a rolling symmetric missile.¹² The horizontal and vertical components of the AoA, β and α , as a function of the range coordinate, s , are fit using the following model. This model contains 10 coefficients that are determined during the fitting process.

$$\beta + i\alpha = K_1 \exp^{i\phi_1} + K_2 \exp^{i\phi_2} \quad (3)$$

$$\phi_1 = \phi_{1o} + \phi'_1 s + 0.5\phi''_1 s^2 \quad (4)$$

$$\phi_2 = \phi_{2o} + \phi'_2 s + 0.5\phi''_2 s^2 \quad (5)$$

$$K_1 = K_{1o} \exp^{\lambda_1 s} \quad (6)$$

$$K_2 = K_{2o} \exp^{\lambda_2 s} \quad (7)$$

The model uses complex variables to describe the instantaneous value of the AoA along the trajectory. The horizontal and vertical components of the AoA, β and α , lie along the real and imaginary axes, respectively. The yawing motion is represented by the sum of two vectors in the complex plane. The magnitude of these vectors is K_1 and K_2 , respectively. The initial amplitude of these vectors at the muzzle is represented by the two coefficients, K_{1o} and K_{2o} . The magnitude of K_1 and K_2 changes in-flight due to the damping rates, λ_1 and λ_2 . The location of the two vectors in the complex plane is determined by the instantaneous phase in the complex plane, ϕ_1 and ϕ_2 . ϕ_1 and ϕ_2 are described in terms of the six parameters, ϕ_{1o} , ϕ_{2o} , ϕ'_1 , ϕ'_2 , ϕ''_1 , and ϕ''_2 .

A nonlinear least-squares-fitting procedure was utilized to fit the measured data points to the theoretical motion. Several combinations of the 10 coefficients were utilized during fitting process. A six-parameter reduction that models the yawing motion of a nonrolling symmetric missile was found to give the most consistent fits to the experimental data and was eventually used to reduce most of the yaw card data. This six-parameter fit assumes that the two damping rates, λ_1 and λ_2 , are equivalent. As a result of the assumption of zero-roll rate, the two frequencies, ϕ'_1 and ϕ'_2 , are equal in magnitude, but opposite in sign. The parameters, ϕ''_1 and ϕ''_2 , which are used to model a linear variation of roll rate with range, are assumed to be zero in the six-parameter reduction. For the six-fin fluted-flare configuration (shots 10-16), a five-parameter fit, which assumes the damping rates, λ_1 and λ_2 , are zero, was used because the yawing motion was measured over a short range with few yaw cards.

An example of the fitted equations to the data for both the horizontal (β) and vertical (α) components of yaw is shown for shot 24 in Figure 12. The circles represent the data measured from the yaw cards, while the curve fit is represented by the solid (β) and dashed (α) lines.

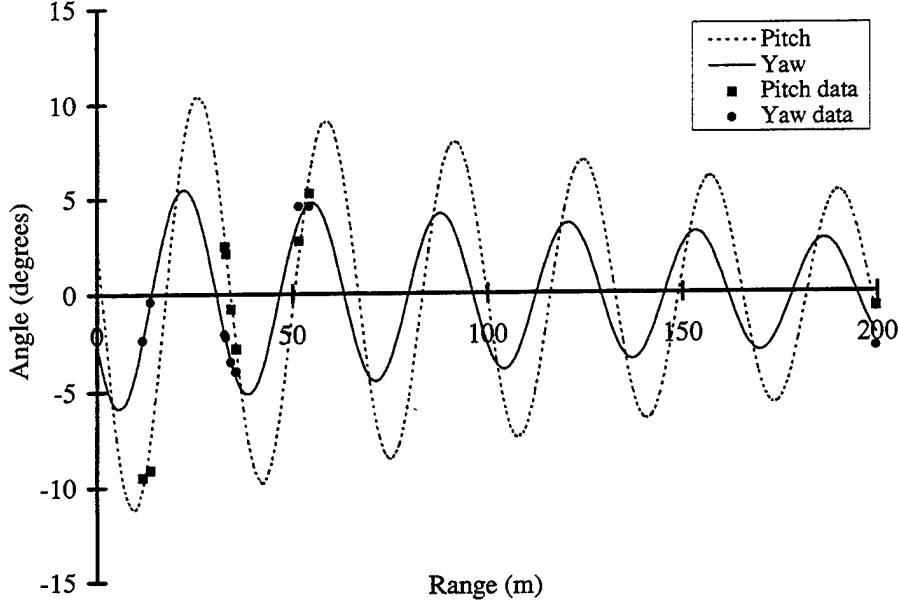


Figure 12. Fit of the measured angular motion from shot 24, α - dashed line, β - solid line.

From the fit of the measured motion, two of the aerodynamic coefficients that have an important role in the vehicle's flight performance were extracted. The pitching moment coefficient derivative, C_{m_α} , which is a measure of the projectile's static stability, is primarily a function of the pitching rate of the projectile. The pitch-damping coefficient, $C_{m_q} + C_{m_{\dot{\alpha}}}$, is related to the damping of the yawing motion and can be determined from the measured damping rates. The dependence of these two coefficients on the measured pitching frequencies and damping-rates is shown below.¹²

$$C_{m_\alpha} = (\phi'_1 \phi'_2 - \lambda_1 \lambda_2) \frac{2I_t}{\rho S_{ref} D^3} \quad (8)$$

$$C_{m_q} + C_{m_{\dot{\alpha}}} = -\frac{I_t}{m D^2} [(-\lambda_1 - \lambda_2) \frac{2m}{\rho S_{ref} D} - C_{N_\alpha} - 2C_D] \quad (9)$$

To extract the aerodynamic coefficients from the measured rates, the physical properties of the body are required. These include the transverse moment of inertia, I_t , the reference area of the body, $S_{ref} = \pi D^2/4$, the body diameter, D , the body mass, m , and the atmospheric air density, ρ . The measured physicals for both types of subprojectiles are listed in Table 7. The determination of the pitch-damping coefficient from the measured

Table 7. Physical Properties of Subprojectile.

	Six-fin	Four-fin
Axial Moment of Inertia, I_x (g-cm ²)	5.137	6.345
Transverse Moment of Inertia, I_t (g-cm ²)	1486.6	1506.3
Mass, m (g)	84.61	85.92
Total Length, L (mm)	173.26	176.71
Axial Position of c.g. - from nose (mm)	85.66	85.36
Reference Diameter, D (mm)	7.22	7.22

damping rates requires the normal force coefficient derivative, C_{N_α} , and the drag coefficient, C_D . These coefficients were determined using theoretical methods discussed in section 3.2.

In a relative sense, the pitching moment coefficient derivative will be more accurately determined from the yaw card data than the pitch-damping coefficient because the frequencies of the yawing motion are more easily determined than the damping rates. Generally, good damping data requires that the amplitude of the pitching motion be measured over several cycles of the motion, while the frequency can be obtained from the period of the yawing motion using fewer measurements over a shorter range.

The best results for assessing the aerodynamic coefficients from yaw cards are obtained when the measured angles are greater than 2° and less than 10°. The minimum requirement is a result of interpreting small angles from the yaw card impacts. At high AoAs (approximately 10° and up), the aerodynamics may become nonlinear and the aerodynamic coefficients (particularly C_{m_α}) could exhibit a dependence on yaw. It is possible to determine the yaw dependence of the aerodynamic coefficients if multiple firings are performed at similar launch velocities. For this effort, the yaw dependence in the aerodynamic coefficients was difficult to determine due to the lack of data. Thus, the aerodynamic coefficients were determined directly from the damping rates and pitching frequencies for individual shots. Some differences between the aerodynamic coefficients obtained from the high-yaw flights and low-yaw experimental and theoretical results are therefore expected.

3.2 Aerodynamic Predictions

The aerodynamic performance of the flight body was also investigated using Computational Fluid Dynamics (CFD) techniques. Using these techniques, the viscous flow field about the projectile was determined by solving the thin-layer Navier-Stokes equations using the parabolized Navier-Stokes (PNS) technique of Schiff and Steger.¹³ This technique is applicable in the supersonic flow regime and requires that the flow field contain no regions of flow separation in the axial direction. Because the computational approach requires only a single sweep through the computational grid, it is very efficient compared with time-marching

approaches that require many sweeps through the grid. The technique has been applied successfully to a number of projectile configurations, including axisymmetric shell,^{14, 15} flared projectiles,¹⁶ and finned projectiles.¹⁵ More recent extensions to the computational approach permit predictions of the pitch-damping aerodynamic coefficients.^{17, 18, 19}

Several simplifications to the flight body were made during the modeling process. A sharp nose tip was modeled instead of the blunted nose tip actually used on the flight body. Predictions for previous versions of this projectile showed little influence of nose bluntness on the aerodynamics for nose bluntness at or below the current value. The actual flight body had a number of subcaliber sabot grooves on the body. These were not modeled in the computation. Finally, the base flow was not modeled. Because the flow is supersonic, the base flow will have virtually no influence on any of the aerodynamic coefficients with the exception of the drag coefficient. However, estimates of the base drag contribution were made and added to the forebody drag to obtain predictions of the total drag of the projectile.

The aerodynamic forces and moments were extracted from the computed flow field by integrating the pressure and viscous stresses at the body surface. Predictions were made of the pitching moment and normal coefficient derivatives, drag coefficient and pitch-damping moment coefficient. Where possible, predictions were validated with comparison with data obtained from the range firings.

3.3 Aerodynamic Performance of the Subprojectile

From the measured yawing frequency, an important measure of the projectile's static stability, the pitching moment coefficient derivative (C_{m_α}), was extracted and compared with the predictions. In Figure 13, C_{m_α} is plotted as a function of velocity for the AoA magnitudes between 2° and 10°. In general, good agreement is found between experiment and theory, and the results show a decrease in the subprojectile's stability with increasing velocity due to the decreased efficiency of the fins at higher velocity. Data from one of the six-fin fluted-flare firings (shot 15) are included and show the improvement in aerodynamic performance of the subprojectile employing the finned afterbody compared to the original fluted-flare design.

On several firings after shot 27, radar was used to obtain the round's velocity as a function of range.²⁰ From this data, the subprojectile's retardation and drag coefficient (C_D) are computed. The experimentally determined drag coefficients include the effect of yaw drag. Attempts to extract the yaw drag from the zero-yaw drag were not successful, due to the variability in the experimental measurement of the total drag. A plot of the reduced radar data from shot 30 is shown in Figure 14. The free-flight velocity profile for both the subprojectile and the armature are indicated. Even with the radar unit in close proximity to the EML, very little triggering problems were experienced with the radar unit.

Comparisons between predicted and measured drag coefficients are shown in Figure 15. Also included is a data point from a subscale firing²¹ at the ARL Aerodynamics Range (solid circle), as well as the PNS prediction for the subscale projectile. The theoretical approach is a reasonable assessment of the expected performance of the subprojectile. The results indicate that the velocity of the projectile will decrease at a rate of 150–200 m/s/km.

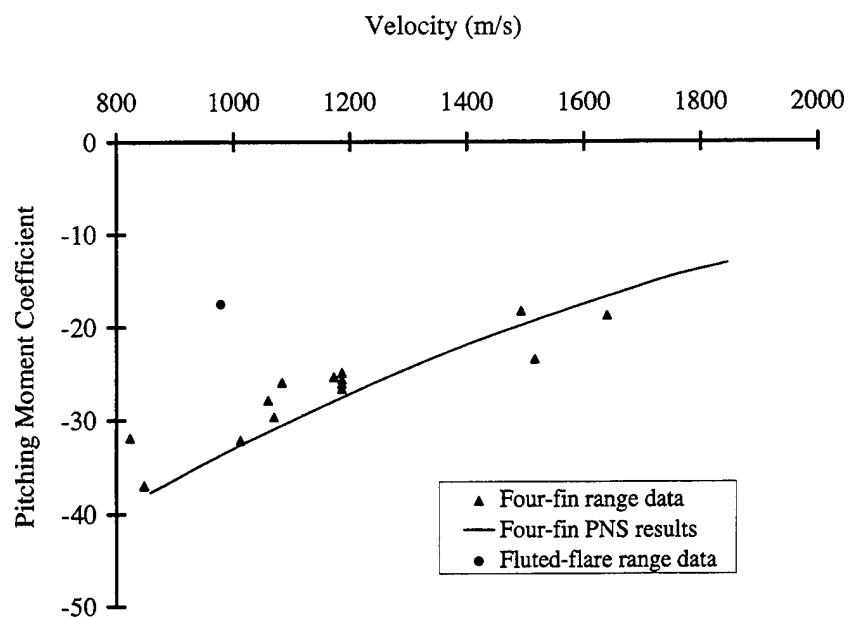


Figure 13. Pitching moment coefficient, $C_{m\alpha}$, as a function of velocity.

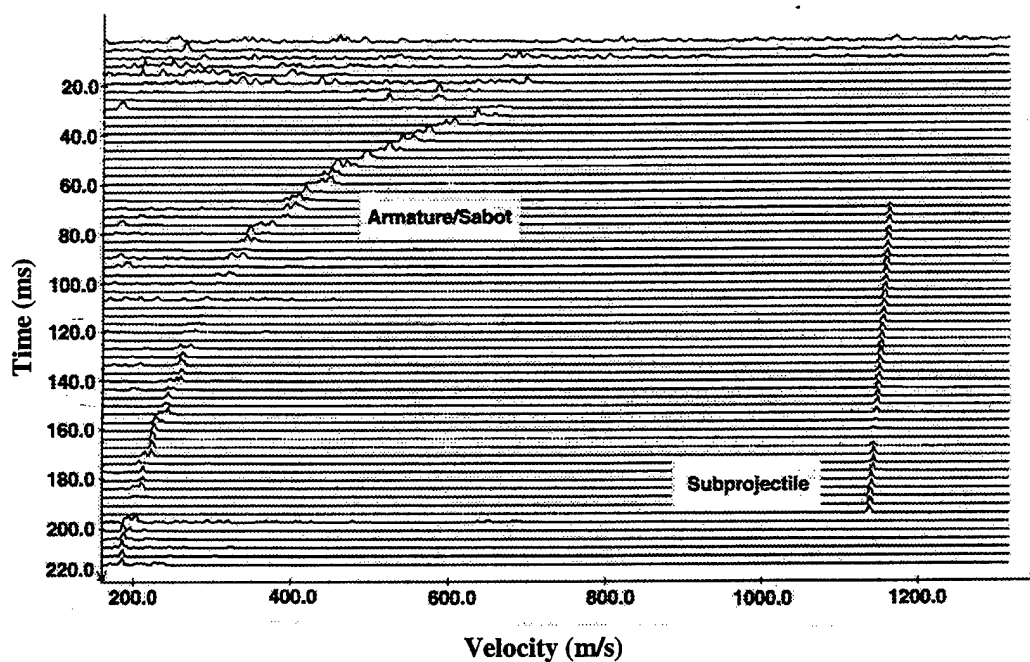


Figure 14. Waterfall plot radar indicating velocity history of subprojectile and armature/sabot.

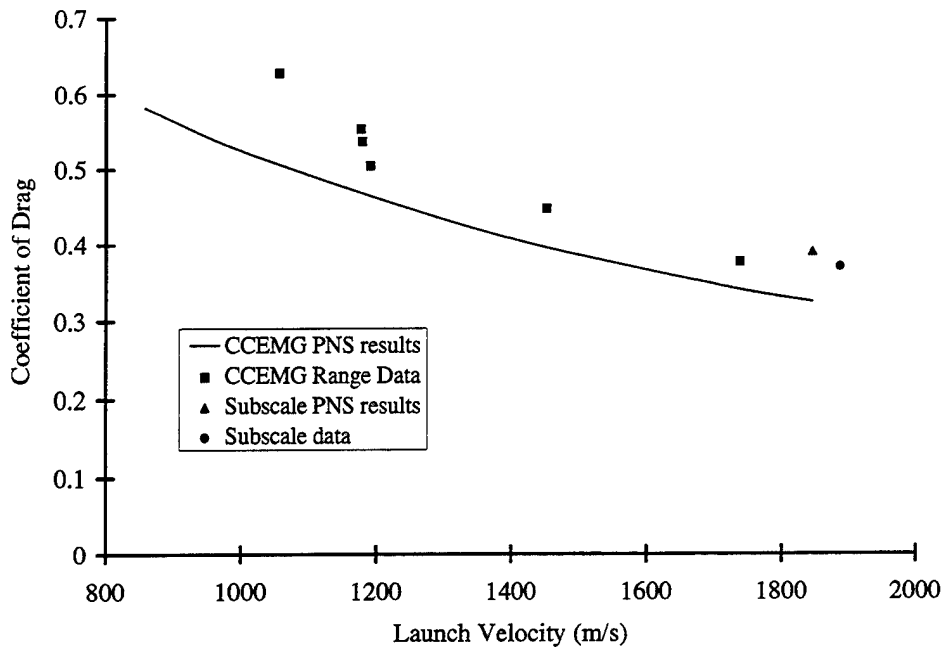


Figure 15. Coefficient of drag, C_D , as a function of velocity.

Predictions of the normal force coefficient derivative were also made and are shown in Figure 16. The normal force coefficient derivative is a vital piece of data required to extract the pitch-damping coefficient from the damping rates and is required to assess the aerodynamic jump of the projectile. Unfortunately, it requires extensive testing to determine the normal force coefficient derivative from the yaw card data, and, hence, no experimental data is shown. However, previous predictions^{16, 22} of the normal force coefficients derivative for similar projectile geometries have shown good agreement with aerodynamic range data leading to confidence in the predicted results.

The measured damping rates, obtained from the fits of the yawing motion, were utilized to determine the pitch-damping coefficient. As shown in equation (9), the extraction of the pitch-damping coefficient from the measured damping rates requires the values of two additional aerodynamic coefficients, namely the normal force coefficient derivative, C_{N_α} , and the drag coefficient, C_D . These values were obtained from the computational predictions and account for about 15% of the experimentally derived pitch-damping coefficient. The pitch-damping coefficients extracted from the measured damping rates were compared with CFD predictions of the pitch-damping coefficients. The measured pitch-damping coefficients show considerable scatter, but generally bracket the computational predictions. The predicted pitch-damping coefficient, shown in Figure 17, shows a small decrease with Mach number. Both the experimental data and theoretical predictions indicate that the aerodynamic damping performance of the body will cause the amplitudes of the yawing motion to damp to less than 10% of their initial amplitudes after 500 m of flight.

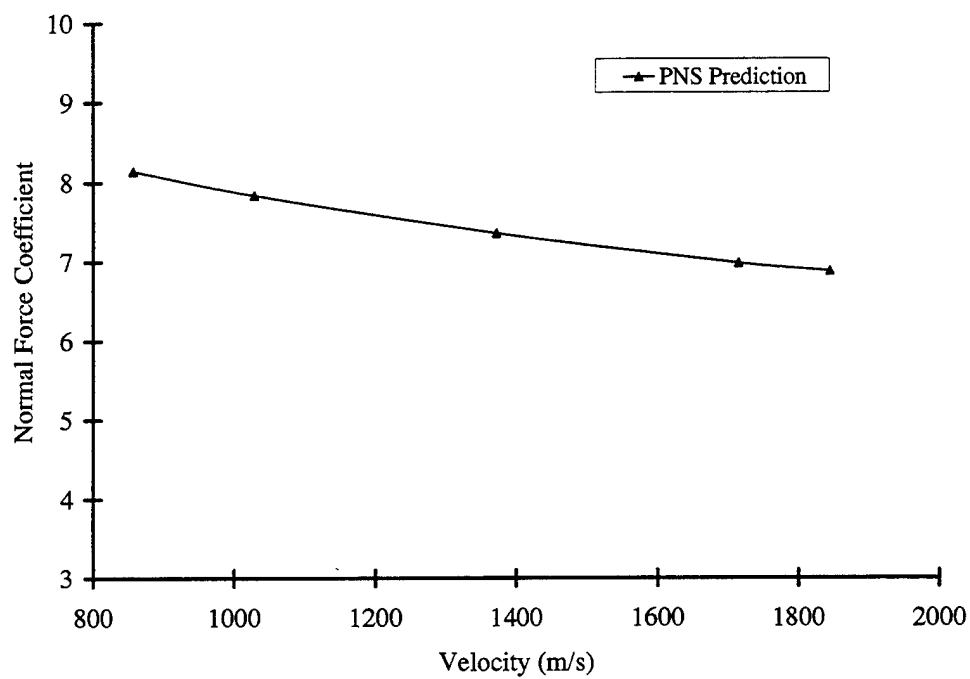


Figure 16. Normal force coefficient, C_{N_α} , as a function of velocity.

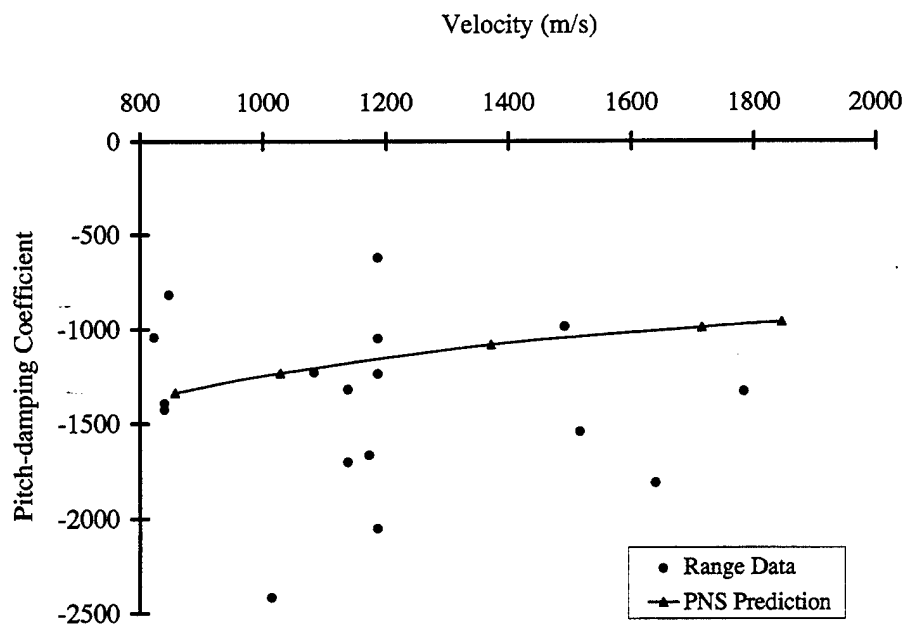


Figure 17. Pitch-damping coefficient, $C_{m_q} + C_{m_{\dot{\alpha}}}$, as a function of velocity.

3.4 Reduction of the Swerving Motion

In addition to measuring the free-flight angular motion, the vertical and horizontal displacement of the subprojectile center of gravity was also measured. The motion of the projectile center of gravity (swerving motion) is characterized by three effects: (1) vertical gravity drop, (2) horizontal and vertical linear deviation off the original aim point (jump), and (3) horizontal and vertical fluctuating displacements due to the aerodynamic response of the body to the yawing motion. The maximum peak-to-peak amplitude of the fluctuating motion was less than 3 mm per degree of yaw. Because amplitude of the fluctuating motion was on the order of the measurement error of the center of gravity displacement obtained from the yaw cards, no attempt was made to fit the fluctuating motion. However, the linear deviation of the c.g. from the original aim point was utilized to assess the jump performance of the projectile, as discussed in the following section.

4. Jump

4.1 Jump Description

The flight path of the subprojectile, and, hence, the accuracy and dispersion, is influenced by the series of launch disturbances leading up to free flight. For direct-fire weapon systems, the launch process can be described as a series of six disturbances from shot start to the impact of the round at the target.²³ Each of these disturbances produce horizontal and vertical deflections of the subprojectile from the intended line of fire. The first three disturbances result from the motion or distortion of the gun tube during the firing cycle. The first deflection is produced by the pointing angle of the muzzle at projectile exit (PA). At the same time, the motion of the muzzle imparts a transverse velocity or crossing velocity to the projectile (CV). The third component is the angular deviation of the flight path of the projectile's center of gravity relative to the instantaneous bore centerline at projectile exit (CG). Shortly after projectile exit, the armature/sabot discards or separates from the subprojectile producing an additional launch disturbance (SD). As the subprojectile enters free flight, the aerodynamic forces produce an average deflection due to the angular rates produced by previous four launch disturbances. This resultant deflection is called aerodynamic jump (AJ). The final deflection of the subprojectile is due to gravity drop (GD).

The aerodynamic forces acting on the subprojectile will produce oscillations about the mean flight path due to the pitching motion, although these deflections are usually small. Of greater concern is the average deflection of the subprojectile from its intended flight path. With the exception of gravity drop, which produces a parabolic deflection in the flight path, the launch disturbances produce an angular deviation of the flight path from the intended line of fire such that the vertical and horizontal deflections from the intended flight path increase in a linear manner as the subprojectile flies downrange. These linear deviations are referred to as "jump" and are typically expressed in unit of mils. (One mil is 1 unit of deflection at 1,000 units of range.) The six individual jump components in the kinetic energy projectile jump model can be vectorily added, and the resulting total subprojectile jump should be in good agreement with the measured deflection at the target from the original

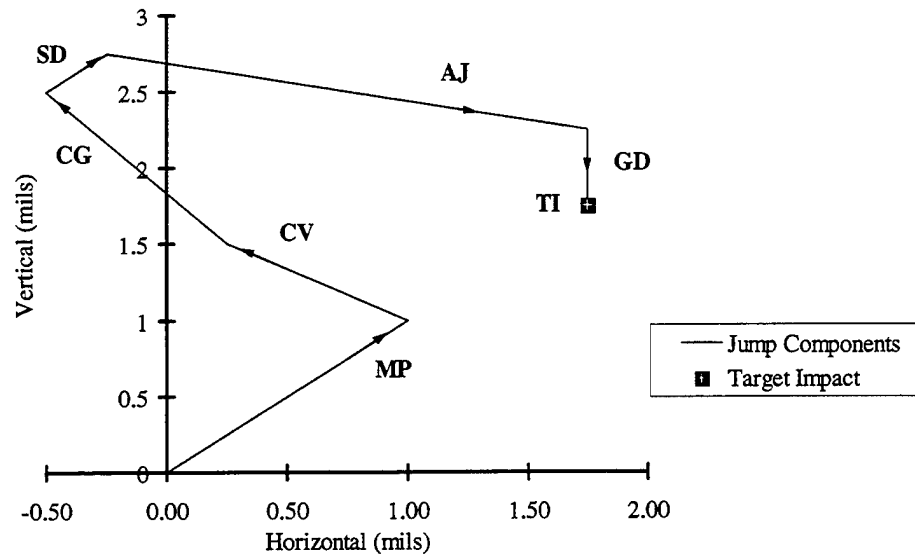


Figure 18. Schematic depiction of jump components from aim point to target impact.

aim point if the jump components are accurately measured. (See Figure 18.)

Each of the jump components is the result of forces acting on the subprojectile. The forces result in jump vectors and angular rates when they are applied to masses and center of gravity locations. Understanding the source of the forces acting on the subprojectile and their interaction can lead to significantly enhanced accuracy and reduced dispersion. It is not the intent to predict the accuracy or dispersion in this section, but rather to isolate physical processes that contribute toward the target impact dispersion.

4.2 Jump Component Determination

The individual jump components are experimentally determined by measuring the motion and orientation of the launcher, ILP, and subprojectile during the various phases of the launch and flight process. The total jump vector due to the CV, PA, and CG jump components was determined from the round's center of gravity trajectory at muzzle exit relative to the fiducial system in the multistation orthogonal x-rays. A straight line is fit to the center of gravity locations as a function of range for each plane, and the slope of the line is the total jump vector due to the CV, PA, and CG jump components. An example of a multistation, orthogonal flash x-ray image with fiducial cable is shown in Figure 19.

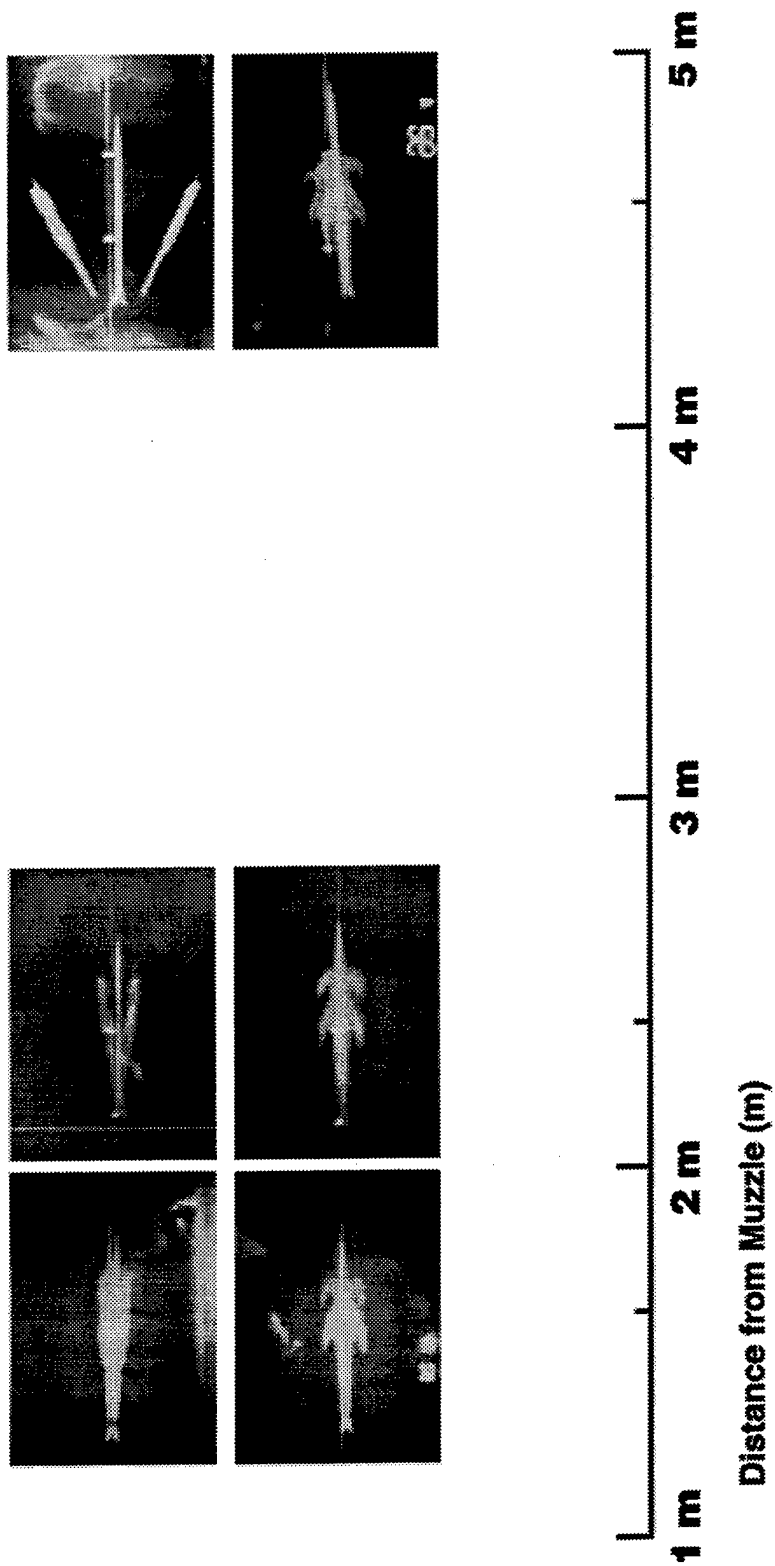


Figure 19. Multistation, orthogonal flash x-ray images from shot 26 (launch velocity = 1,087 m/s).

For the work presented here, instrumentation was not available to monitor the transient motion of the muzzle; however, the launcher was firmly bolted to a steel frame at the breech end and supported 0.6 m from the muzzle end. The frame was bolted to steel channel embedded in the concrete floor. Additionally, the aim point of the launcher relative to the target located at 222 m was checked periodically by boresight and found not to change between shots. Hence, it is assumed that the CV and PA jump vectors are negligible. The jump vector determined directly from the orthogonal x-rays at muzzle exit is attributed to the CG jump vector as defined in the model.

The AJ jump component describes the mean deviation of the flight path due to the aerodynamic forces acting on the projectile in free flight. For a symmetric, nonspinning projectile, the aerodynamic jump in the vertical (AJ_v) and horizontal (AJ_h) planes can be computed as:¹²

$$AJ_v = -1000 \frac{I_t C_{L\alpha}}{m D C_{m\alpha}} (\alpha'_o + \frac{H}{D} \alpha_o) \quad (10)$$

$$AJ_h = -1000 \frac{I_t C_{L\alpha}}{m D C_{m\alpha}} (\beta'_o + \frac{H}{D} \beta_o) \quad (11)$$

$$H = \frac{\rho S_{ref} D}{2m} [C_{L\alpha} - C_D - \frac{m D^2}{I_t} (C_{m_q} + C_{m_{\dot{\alpha}}})] \quad (12)$$

$$C_{L\alpha} = C_{N\alpha} - C_D \quad (13)$$

$$\alpha'_o = \left. \frac{d\alpha}{ds} \right|_o \quad (14)$$

$$\beta'_o = \left. \frac{d\beta}{ds} \right|_o \quad (15)$$

The subprojectile transverse moment of inertia (I_t), diameter (D), and mass (m) are measured quantities that are listed in Table 7. The aerodynamic coefficients $C_{L\alpha}$, $C_{m\alpha}$, and $(C_{m_q} + C_{m_{\dot{\alpha}}})$ are obtained from the CFD predictions. (The pitching moment and the pitch-damping coefficient derivatives could be obtained experimentally from the fits of the yawing motion. Some variability in the measured aerodynamic coefficients was observed, particularly for the pitch-damping coefficient. The CFD predictions of $C_{m\alpha}$ and $(C_{m_q} + C_{m_{\dot{\alpha}}})$ provided a more consistent assessment of the aerodynamic coefficients and were therefore used.)

The vertical and horizontal components of the AoA when the projectile enters free flight, α_o and β_o , and the associated angular rates, α'_o and β'_o , were determined from the fit of the yawing motion for each shot. Analysis of the x-ray and yaw card data indicated that the sabot discard was complete by 4.5 m from the muzzle. This location was used to evaluate the necessary AoAs and angular rates for the AJ computation. The sensitivity of the aerodynamic jump to the selection of the range location where the projectile entered free flight was analyzed. The results indicated that the aerodynamic jump varied on the average by about $\pm 5\%$ for a ± 0.5 -m variation in the range location. This variability is quite small in relation to the shot-to-shot variability in AJ. Additional analysis indicated that the angular rate term accounted for nearly all of the aerodynamic jump when compared to the AoA term in equations (10) and (11). Both terms, however, were included in the computation presented here.

The parameters in equations (10) and (11) should be computed in a consistent set of units, and the angles should be evaluated in radians. By adding the multiplicative factor of 1,000 in equations (10) and (11), the AJ will be computed in mils. The direction of positive jump in each plane will be in the direction of positive yaw for each plane.

The gravity drop of the projectile as a function of range, R , was computed using the measured launch velocity, V .

$$g_{drop} = \frac{1}{2}g \left(\frac{R}{V} \right)^2 \quad (16)$$

The gravitational constant, g , is 9.81 m/s^2 . This form of the gravity drop assumes that changes in the velocity during flight are negligible. The instantaneous deflection of the trajectory from the original line of fire in units of mils (or jump due to gravity drop) can be determined from the gravity drop.

$$GD = 1000 \frac{1}{2}g \left(\frac{R}{V^2} \right) \quad (17)$$

For fielded weapon systems, a shot-to-shot variability in gravity drop produced by variations in launch velocity is often considered. Because the launch velocity is purposely varied in the current program, a shot-to-shot variability or dispersion due to gravity drop is not considered. The computation of the vertical deflection due to gravity drop is required for each shot to extract the individual jump components.

In the work presented here, it was not possible to directly determine the jump components due to the sabot/armature discard. Since each of the other jump components have been determined and the aim point and target impact locations have been measured, the SD vector was taken to be the vector required to close the jump diagram between the CG component and the AJ component. (Refer to Figure 18.)

Figure 20 shows a four-component jump vector diagram for shot 26 using yaw card impact data 35 m downrange. The four components evaluated are CG, SD, AJ and GD. The aim point is located at (0,0), and the impact at the target is denoted TI. Also shown is a launch dynamics jump vector (LD), which is constructed from the origin to the AJ vector. The LD vector essentially contains the combined effects of the CG and SD jump vectors. While it is desirable to consider both the CG and SD jump vectors independently, multistation orthogonal flash x-rays were not available after shot 27, and the CG jump vector could not be determined. The LD jump vector was utilized to allow an analysis of the jump data for all of the shots, particularly to examine the trends of the AJ and LD components relative to the target impact dispersion at high muzzle velocity where multistation x-ray images were not available. As shown in Figure 20, the LD vector indicates that the combined CG and SD disturbance is primarily in the vertical direction and is larger than the AJ component. Similar plots were made for all shots.

Once the jump vector diagrams were assembled, the bias (mean) and dispersion (standard deviation) of the individual jump components were determined. Statistical analysis was performed on the horizontal and vertical components of the individual jump vectors. Because of the geometry of the railgun and armature/sabot (the conducting rails above and below the ILP, the insulated sidewalls to the left and right of the ILP, and the plane of

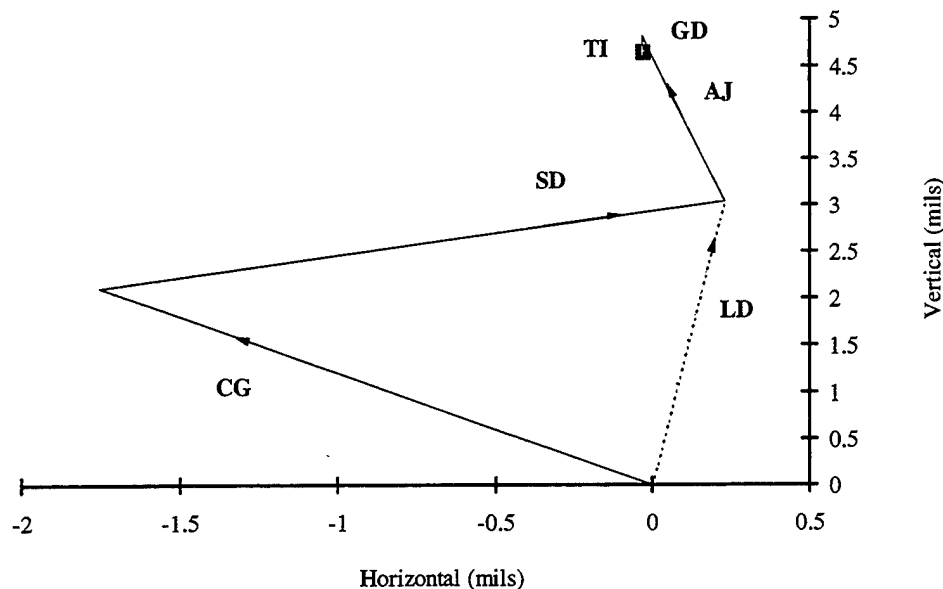


Figure 20. Jump vector diagram for shot 26.

separation for the armature/sabot oriented vertically), differences in the vertical and horizontal behavior of the jump components could be expected.

An understanding of the statistical behavior of the individual jump components is important for improving the target impact accuracy and dispersion. The bias and dispersion of the individual jump components can be related to the target impact bias and dispersion. The sum of the biases of the individual components is equal to the bias of the target impact location. A more complicated relationship between the target impact dispersion and the individual component dispersions exists. If the individual jump components are independent of each other and the data is normally distributed (in a statistical sense), the square root of the sum of the individual jump component dispersions squared should equal the target impact dispersion (TI). Differences are attributed to measurement errors and the dependency between components. This dependency or "cross correlation" can exist statistically and physically, and can be either negligible, constructive or destructive.²³ In general, cross correlations are not desirable and negative cross correlations should not be relied on to reduce the dispersion in a gun system. For low-dispersion, high-accuracy systems, it is desirable to produce small magnitude jump components. Large dispersions in individual jump components can lead to unacceptable round-to-round dispersion. Additionally, small individual jump component dispersions originating from large magnitude jump vectors can lead to unacceptable target dispersions because of the increased potential for significant cross correlations between individual jump components.

4.3 Bias and Dispersion of the Jump Components

A statistical analysis of the jump component data obtained from the firings of the four-fin subprojectile (shots 17–39) was performed. For five shots (shots 20, 24, 25, 26, and 27), x-ray data at the muzzle were available, and four component jump diagrams (CG, SD, AJ, and GD) could be constructed. The muzzle velocities for these five shots ranged from 826 m/s to 1087 m/s. The statistical analysis of the jump components revealed a consistent bias in only one of the jump components, the CG jump. The average location of all the CG vectors is 2.40 mils above and 1.34 mils to the left of the intended line of flight. A potential contributing cause of the bias in the CG jump is the deviation of the bore centerline of the launcher. Figures 21 and 22 show the measured deviation of the launcher centerline along the length of the launcher in the horizontal and vertical directions near the muzzle. The deviation of the centerline appears to be oriented in the same direction as the CG jump. It is important to note that the muzzle pointing direction, as established by the borescope, does not fully account for the displacement in the bore centerline very close to the muzzle, since the borescope makes contact with the bore conducting rails and sidewalls approximately 1.7 m and 2.0 m from the breech. The bias in the CG jump also appears to be correlated to the bias in the target impact location. The average impact location at 30 m for these five shots is 2.08 mils above and 0.37 mils to the left of the intended line of flight. These data suggest that this launcher has an interior ballistic, dynamic path that consistently launches the ILP with this bias. The other jump components did not show a consistent bias of the jump components, particularly when compared to their individual dispersions.

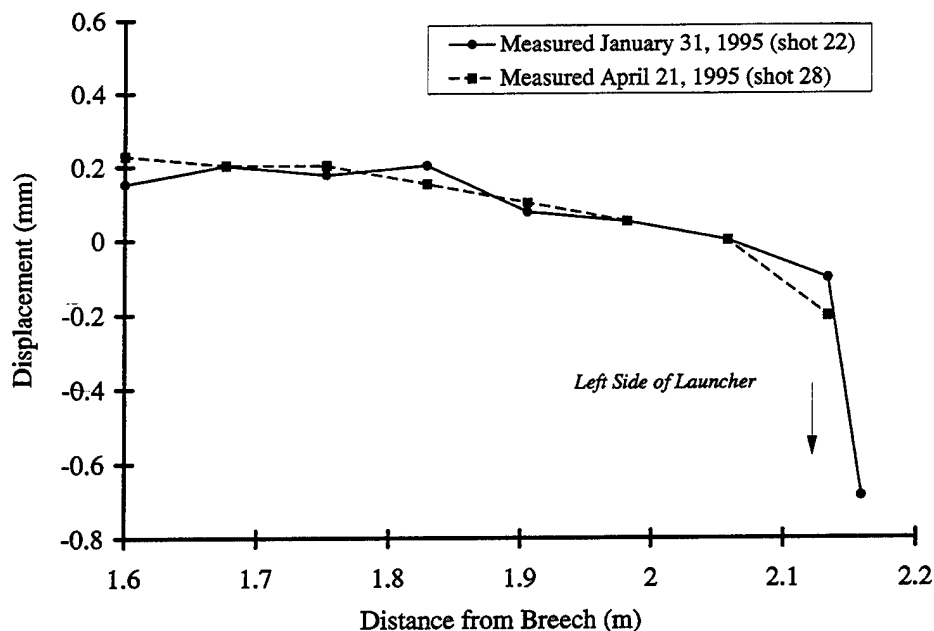


Figure 21. Displacement from bore centerline (horizontal plane).

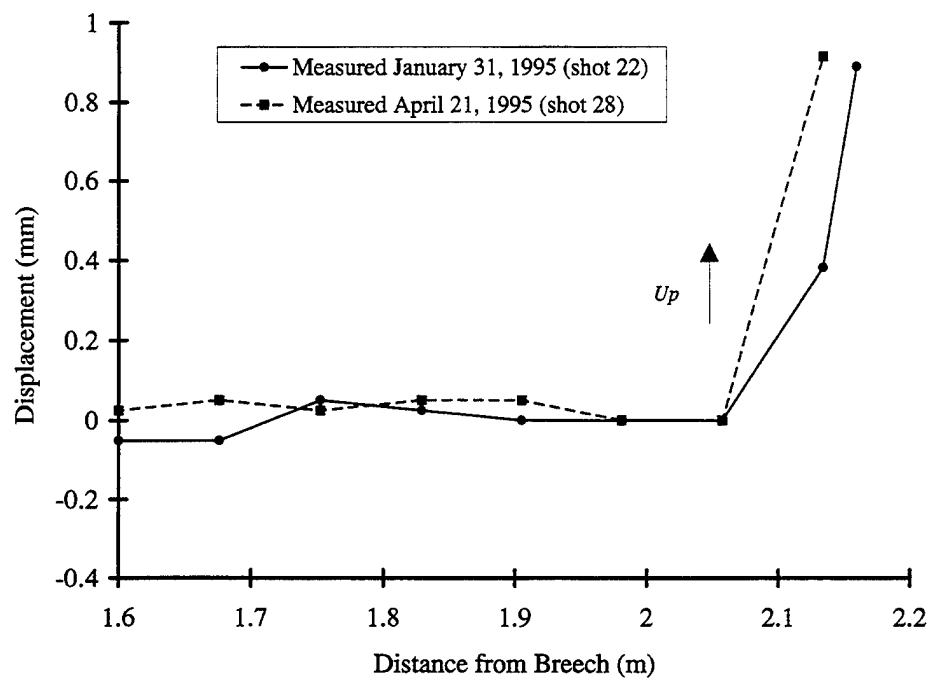


Figure 22. Displacement from bore centerline (vertical plane).

While the bias in the jump components indicates the average or mean behavior of the jump components, it is also very important to consider the variability or dispersion of each jump component. Figure 23 displays the dispersions for AJ, SD and CG for the five shot group where muzzle x-rays were available. AJ and CG jump component dispersions are larger in the vertical plane than in the horizontal plane. The component dispersion due to SD is about 30% larger in the horizontal direction than in vertical direction. Differences in the sabot discard disturbance in the vertical and horizontal planes are not unexpected since the sabot halves are split in the vertical plane and separate from the subprojectile in the horizontal plane.

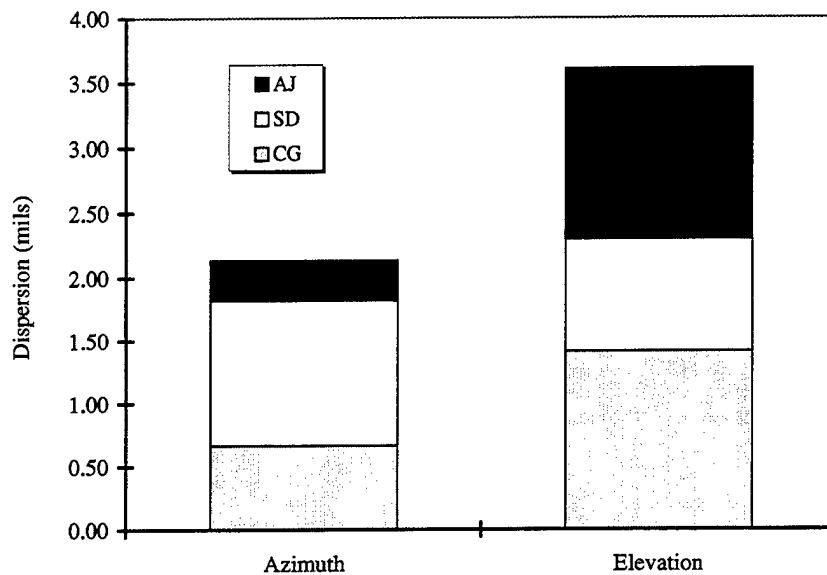


Figure 23. Jump component dispersions (CG, AJ, SD) for shots 20, 24–26, and 27.

As discussed previously, the sum of the squares of the individual jump components should be equal to the square of the target impact dispersion for normally distributed data that exhibits no significant cross correlations. Figure 24 displays the contribution of each jump component dispersion squared as compared to the sum of the squares of the individual component dispersions. In the horizontal plane, the square of the sabot discard dispersion contributes 70% to the sum of the individual dispersions squared. This indicates that if the sabot discard dispersion could be eliminated completely, the target impact dispersion could be reduced to 55% ($\sqrt{1 - 0.70} \times 100\%$) of the current value in the absence of cross correlation. Conversely, relatively little reduction in the target impact dispersion would be expected by eliminating the SD dispersion in the vertical plane, which is dominated by the CG and AJ dispersions.

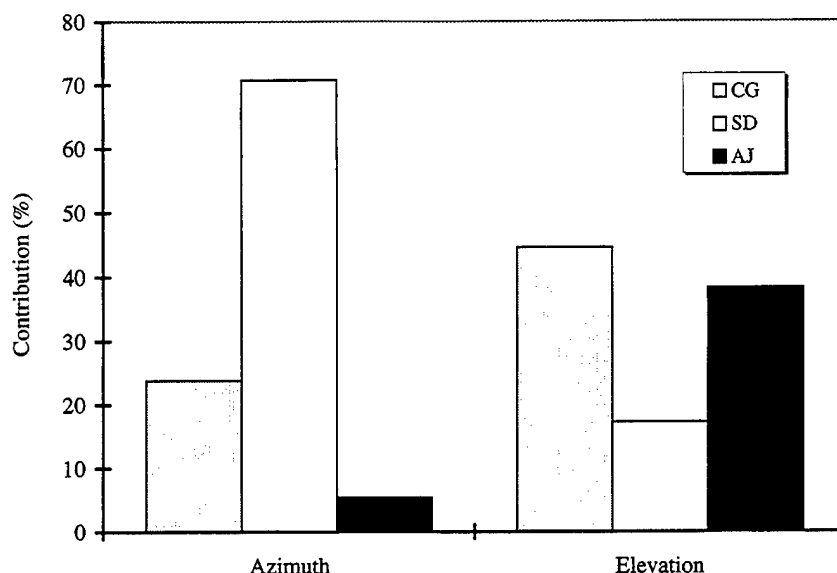


Figure 24. Percentage comparison of jump component dispersions (CG, AJ, SD) for shots 20, 24–26, and 27.

An equivalent LD vector can be constructed from the CG and SD jump vectors for the same group of shots. The resulting dispersion of the equivalent LD vector for this five shot group is 0.71 mil in the horizontal plane and 0.84 mils in the vertical plane. It is interesting to note that the dispersion of the LD jump is less than the dispersion of the SD component alone in the horizontal direction and less than the CG component alone in the vertical direction. This suggests a beneficial cross correlation between the CG and SD dispersions, which reduces their combined effect as represented by the relatively low LD dispersion.

The LD vector was also utilized to analyze the larger set of data, which included shots where muzzle x-rays were not available. As a means of evaluating the jump data as a function of launch velocity, the shots were categorized as either low, medium, or high muzzle velocity. Shots 19, 20, 24, and 27 made up the low muzzle velocity group with muzzle velocities between 825 and 850 m/s. The high muzzle velocity group, which ranged from 1,275 to 1,800 m/s consisted of shots 33, 35, 37, 38, and 39. All other rounds were categorized as medium muzzle velocity, having muzzle velocity between 1,000 and 1,200 m/s. Furthermore, medium muzzle velocity shots were partitioned into two subgroups, according to whether the bore was maintained (i.e., honed) between shots. The first subgroup, medium muzzle velocity "A", consisted of shots 21, 22, 23, 25, and 26, while shots 28 through 32 made up the medium muzzle velocity "B" group.

The dispersion of the AJ and LD components as a function of average launch velocity for shots 19 through 39 is shown in Figure 25. The discontinuity in the plot at 1,100 m/s is at a point in the testing where minor revisions were made to the armature. Changes to the manufacturing procedures included smaller tolerances on the subprojectile driving lands of the armature, a procedural change in machining the armature halves, and an increase to the interference fit (i.e., tighter fit) of the contacts to the bore. The results suggest that tolerances at the interface between the sabot and subprojectile may play an important role

in the mechanical disengagement of the sabot from the subprojectile as the projectile enters free flight. The LD and AJ jump component dispersions are larger in the vertical direction than in the horizontal direction. The general trend appears to indicate an increase in the jump component dispersions with velocity. This trend was also seen in the target impact dispersion. Within either the vertical or horizontal planes, the launch dynamics component dispersion is roughly the same magnitude as the aerodynamic jump component dispersion.

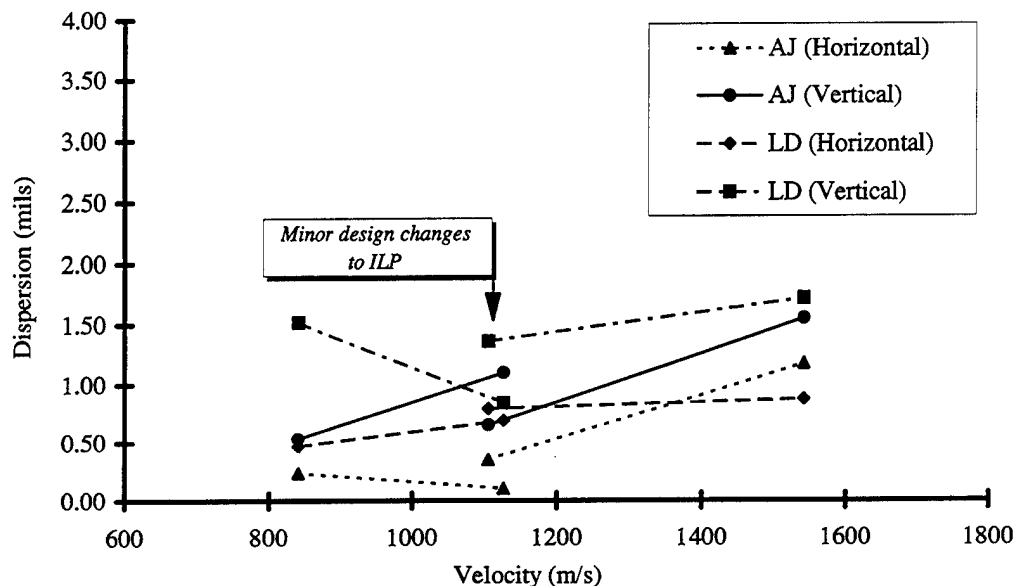


Figure 25. Dispersion for AJ and LD jump components as a function of average launch velocity.

Although the jump components due to sabot/armature discard could not be directly measured, it was possible to qualitatively assess the disturbance due to the sabot/armature discard. In Figure 26, the fitted free-flight yawing motions and the angles as measured in the x-rays for the six-fin configuration are plotted as a function of range. There were no aerodynamic features incorporated on this armature to ensure reliable separation. It is clear that close to the muzzle, but before the armature begins to discard, the angular rates produced by the muzzle launch disturbances would produce an amplitude of 5° according to the fit of the x-ray data. However, shortly after the second x-ray station, the armature separates from the round and the angular rate has changed significantly. By 12 m, the impulse associated with the armature discard at 5 m has begun to manifest itself as a larger amplitude angle as the round enters free flight. Because of the large amplitude in the yawing motion associated with this shot, the effect of the discard was obvious. Design changes made to the separation scoop and rod-armature interface after shot 16 resulted in improved discard.

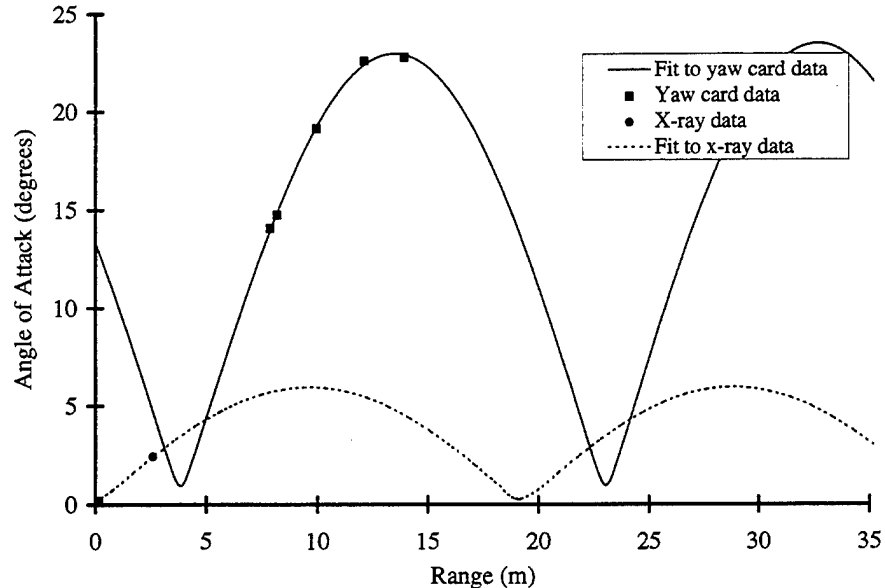


Figure 26. Fitted free-flight (solid line) and muzzle (dashed line) yaw amplitude for shot 16.

Since the barrel is assumed to be rigid, the yawing motion determined by the x-rays is thought to be caused by in-bore balloting forces and deviation from the bore centerline acting on the ILP center of gravity. On the other hand, the yawing motion associated with free flight includes the armature discard event and represents the final angular motion of the round. In Figure 27, the maximum angular rates for shot 25 and 26 are plotted. The free-flight rates are noticeably larger than those measured by the x-rays. This verifies that the discard event is able to produce enough force to significantly alter the round's angular rate just as it enters free flight. Similar observations are made for the velocity group at 826 m/s. On average, 63% of the magnitude of this disturbance is oriented in the vertical direction. It is suspected that the increased disturbance in the vertical direction is initiated by the armature discard in the horizontal direction and transformed by a rotation about the longitudinal axis of the armature halves into a displacement of the subprojectile in the vertical direction. In the time interval between the disengagement of the ILP from the launcher and completion of armature discard, initial angles and angular rates are established in the ILP. In Figure 28, the separation distance between the subprojectile and the front of the armature as a function of range is plotted. The plot includes data from many tests covering a wide range of initial conditions (peak current, exit current, and velocity), as well as different measurement techniques (yaw cards, x-rays, and smear cameras). However, for the first 3.5 m and over a wide range of velocities, the front of the armature has separated less than a few rod diameters away from the body of the rod. Also, the rear of the armature has not started to move away from the rod body until 2.5 m downrange. After 4 m, the slope of the displacement data dramatically changes as the discard event proceeds. The position of each armature half varies very little as a function of range despite the widely varying velocities, exit currents, and initial conditions.

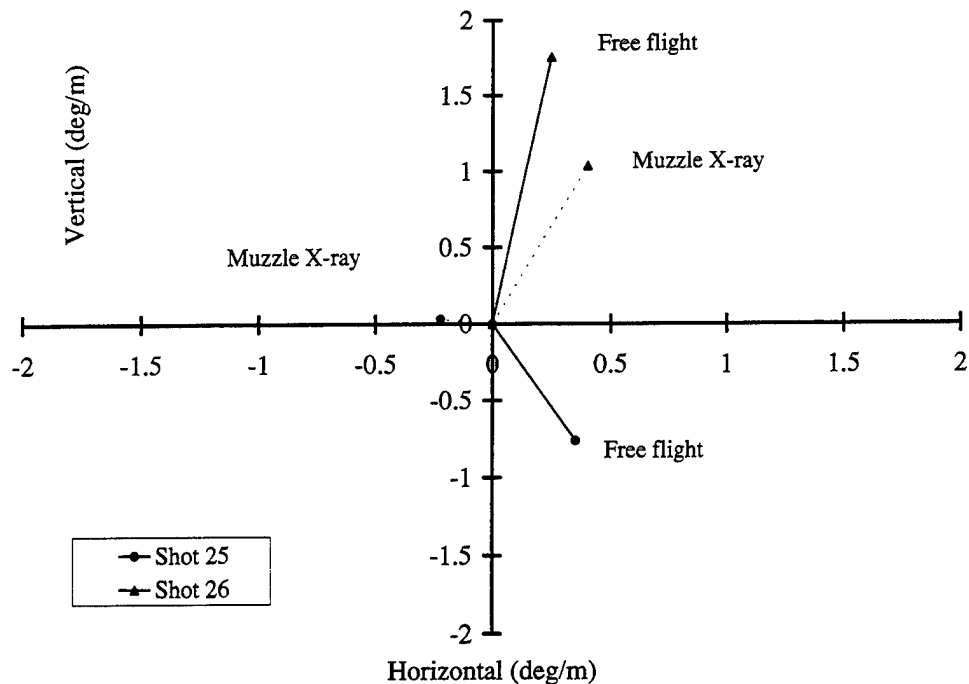


Figure 27. Muzzle and maximum free-flight angular rates for shots 25 and 26.

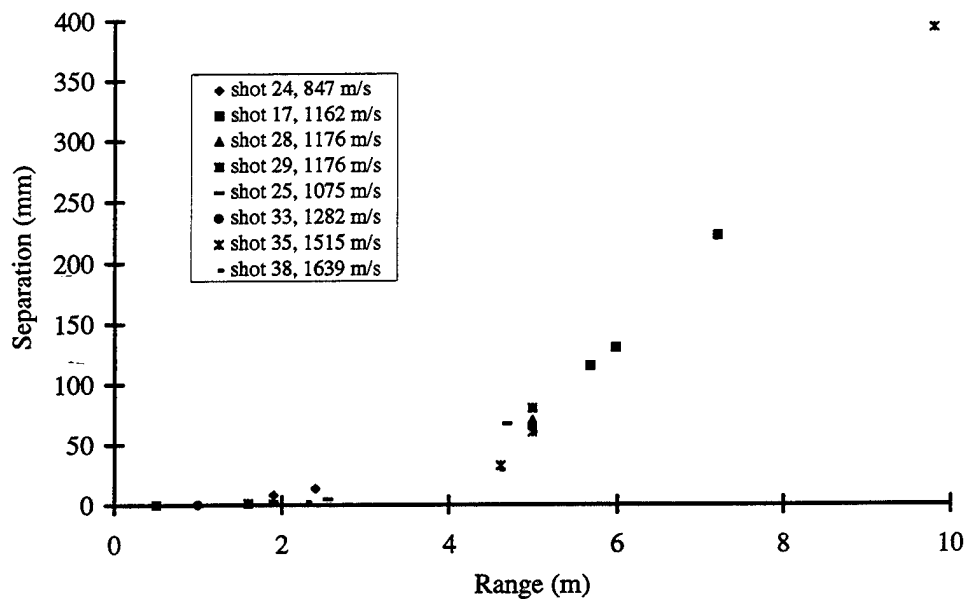


Figure 28. Separation distance between the subprojectile and the front of armature.

5. Target Impact Dispersion and Accuracy

The variability of impact locations on a target is called the round-to-round dispersion. In weapon system analysis, dispersion measures the precision of fire, and large values can significantly degrade a weapon system's lethality. Normally, a weapon system's dispersion and accuracy are evaluated by firing a large number of rounds at targets located at typical engagement ranges. Although the data discussed in this paper does not meet the requirements for a true dispersion and accuracy test, the data can yield valuable information on the potential dispersion and accuracy characteristics related to the launcher and ILP. Such data can be useful in highlighting potential areas for improving the accuracy of the gun system early in its development.

To make maximum use of the available data, all impact points (yaw card and armor plate) in the projectile's flight path are considered to assess dispersion. The impact data for each shot consisted of impact locations in azimuth and elevation at (1) several yaw cards positioned along the projectile's trajectory; (2) a plywood target (shots 24-27 only); and (3) a steel target located at 222 m, although not all shots impacted all the available targets. In general, the dispersion computed at each target was in good agreement with the dispersion computed at the downrange target. For instance, for the medium velocity group "B" (shots 28-32), the horizontal and vertical dispersion computed at the 30 m target was 0.73 mils and 1.75 mils respectively, compared to the horizontal and vertical dispersions of 0.70 mils and 1.99 mils at the downrange target. The effect of gravity (in effect, the dispersion due to variations in launch velocity) was removed from each vertical impact location.

Computation of dispersion at any target (yaw card or armor) requires the impact locations of multiple rounds. Within the same shot group, the round-to-round dispersion estimates at each downrange target were pooled to obtain a more stable overall estimate of dispersion. This pooled estimate was also weighted by target distance, so that farther targets, where the transients from launch have diminished, have greater influence on the calculated dispersion. The formula for each group's pooled round-to-round dispersion estimate, σ_p , is

$$\sigma_p = \sqrt{\frac{\sum d_i(n_i - 1)\sigma_i^2}{\sum d_i(n_i - 1)}} \quad (18)$$

where d_i is the distance to target i , n_i is the number of rounds that impacted target i , and σ_i is the round-to-round dispersion estimate at target station i . In Figure 29, the round-to-round dispersion estimate is plotted as a function of the average muzzle velocity for each of the four shot groups. Similar to the data in the jump survey, the target impact dispersion is larger in the vertical direction and increases as a function of muzzle velocity in both the horizontal and vertical directions. While it is mathematically possible to perform a linear regression analysis on these data to obtain extrapolated estimates of dispersion at 1,850 m/s, such an approach is not recommended for two reasons. First, the error of prediction when using such a small number of points is usually very high. Second, the high muzzle velocity group spans a wider range of muzzle velocities than all other rounds from the other three groups. All information concerning the relationship between muzzle velocity and dispersion

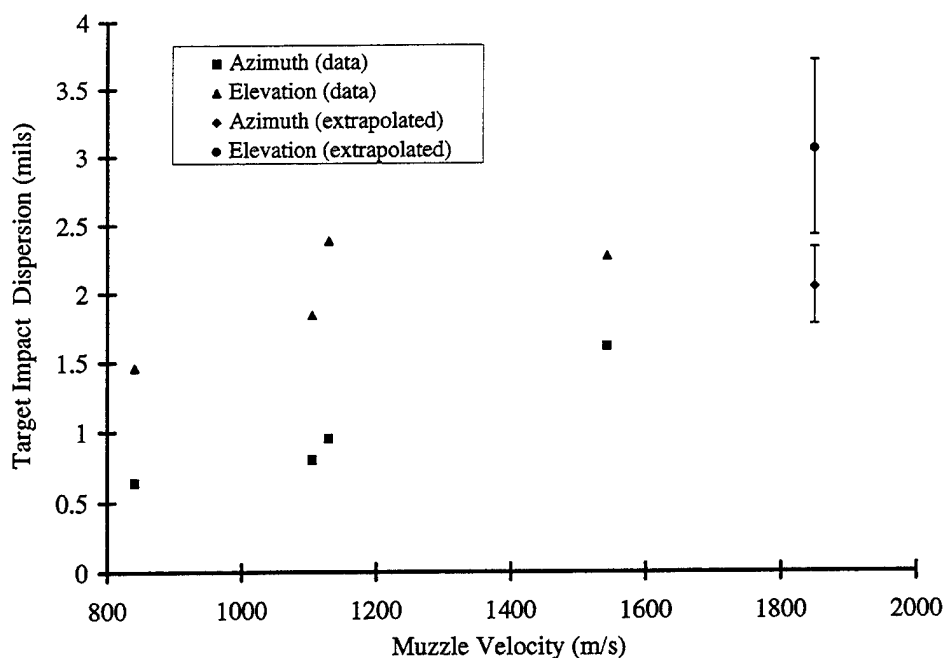


Figure 29. Target impact dispersion in azimuth and elevation (confidence intervals are indicated at 1,850 m/s).

in the 1,200-m/s to 1,800-m/s range is lost when the data are condensed to a single point.

As an alternate approach, each of the four shot groups was partitioned into smaller groups, thus generating more points for the plot of average muzzle velocity versus dispersion. The analysis considered all possible partitions of sizes two and three within each shot group. When forming the partitions, the restriction that no partition could contain shots with muzzle velocities differing by more than 270 m/s is made. Under this rule, 1,890 distinct rearrangements of the data are subjected to a weighted linear regression. This analysis strategy produces a collection of dispersion estimates at 1,850 m/s instead of a single value. Using the 5th and 95th percentiles of these 1,890 values, one obtains 90% confidence intervals. These intervals are (1.8, 2.3) mils in azimuth and (2.4, 3.7) mils in elevation and are indicated in Figure 29, along with the median values of 2.0 mils in azimuth and 3.0 mils in elevation.

The target impact dispersions are much less than the square root of the sum of the squares of the individual jump component dispersions discussed in the previous section. It is suspected that a beneficial cross correlation exists between the jump components, thereby producing a more favorable dispersion at the target. The individual dispersions are nonlinearly coupled and result in a target dispersion that is much smaller than those values shown in Figure 23. Further discussion on cross correlation can be found in Plostins, Celmins, and Bornstein.²³

The accuracy of the subprojectile is measured by its impact location relative to the aim point. The subprojectiles tended to impact to the left of the aim point and were scattered about the aim point in the vertical direction. Statistical regression analysis confirms that

muzzle velocity and impact location data are not related in either direction. Therefore, regardless of the launch velocity, the estimated impact is given by the means of the data, namely, 1.2 mils to the left in azimuth and 0.2 mil upward in elevation.

During shots 28-32, no bore maintenance (honing) was performed, although on the other firings, bore maintenance was performed between shots. An attempt to assess the effect of bore maintenance on the target impact performance was made by comparing target impact performance on shots 28-32 with the performance on previous medium velocity shots (21-23, 25, and 26) where bore maintenance was performed between each shot. Figures 30 and 31 show the vertical and horizontal impact locations for each shot, as well as the mean impact location for each group. The impact dispersion for the two groups is quite similar (0.74 mils and 0.73 mils in the horizontal direction and 1.73 mils and 1.75 mils in the vertical direction for the honed and nonhoned groups, respectively). In the horizontal direction, the deflection from the original aim point is increased by one standard derivation, while the deflection in the vertical is reduced by slightly less than one standard deviation. The data indicate that for the current system fired at medium velocities, the effect of bore maintenance on the target impact dispersion could not be discerned. The effect of bore maintenance may become more apparent with further reductions in the system impact dispersion.

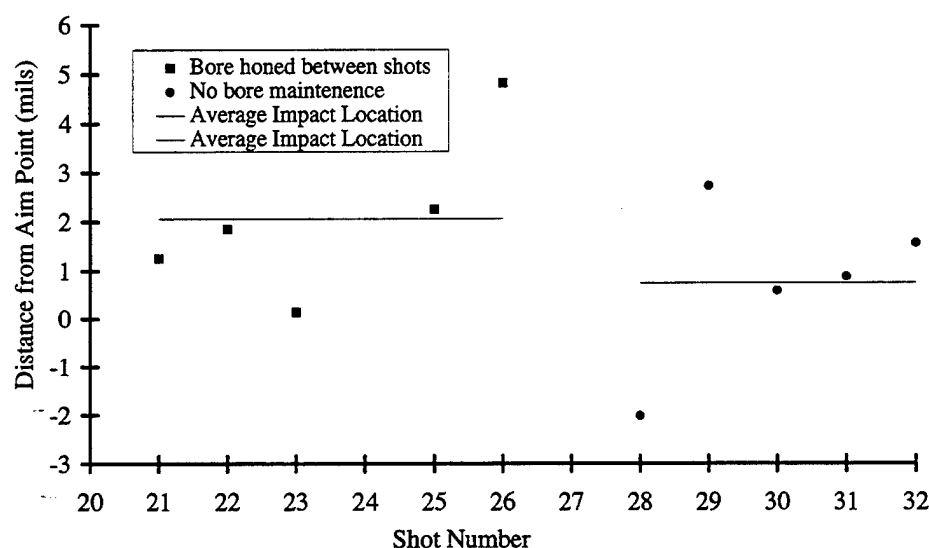


Figure 30. Vertical target impact locations with and without honing between shots, 30-35 m targets.

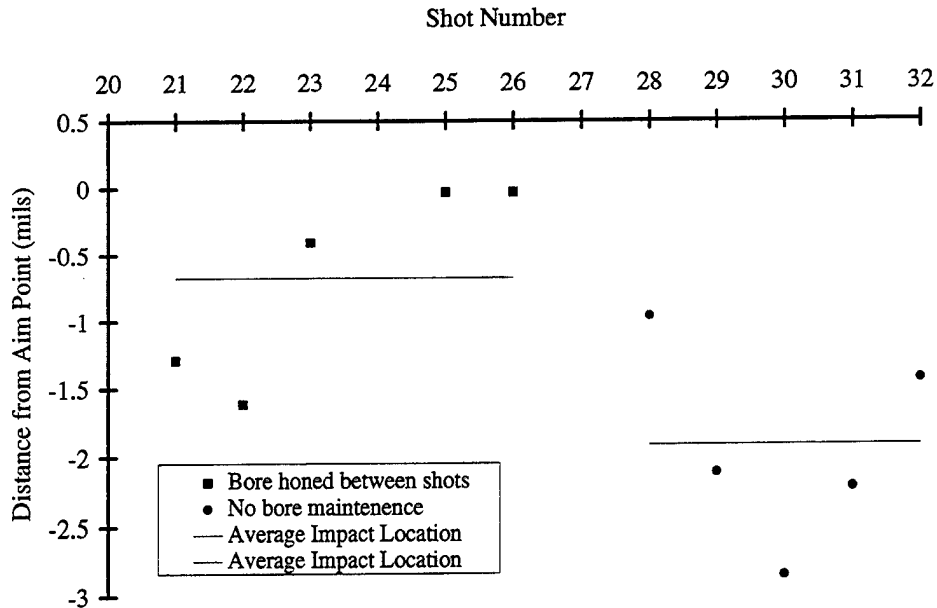


Figure 31. Horizontal target impact locations with and without honing between shots, 30–35-m targets.

6. Terminal Performance

Penetration requirements for CCEMG are given in Table 1.⁹ After shot 27, a high-hard armor (HHA) target assembly was placed downrange just ahead of the 20-mm-thick, mild steel impact target. The armor target consisted of a 32-mm high-hard plate at 60° obliquity. A yaw card was placed directly in front of the HHA target to monitor the AoA at impact. Five of 11 rounds hit the HHA target, producing three partial penetrations (PP) and two complete perforations (CP). Figure 32 shows a front view of the armor plate with the five impacts. The impact data was used to compute an effective value of rolled homogeneous armor (RHA) penetration from the combined HHA and steel.²⁴ Figure 33 shows the expected terminal ballistic performance of the subprojectile as a function of range for zero-yaw impacts. The penetration decreases with range due to the decreasing velocity of the subprojectile. Also shown are the measured data from the five shots that impacted the target. The striking yaw angle is indicated next to the measured data. An effective range location is used for plotting the measured data. This effective range is determined by matching actual impact velocity to the experimentally determined velocity vs. range relationship assuming a launch velocity of 1850 m/s. The measured penetration data is about 17% below the expected terminal ballistic performance because of the projectile's sensitivity to yaw effects at the target due in part to the sharp nose (6° conical half angle). The fit to the impact data with the measured retardation suggests that the round is capable of meeting the penetration-at-range requirements. Data for a medium caliber conventionally launched round is also plotted in the figure. The conventional round penetrates less RHA at the same range as the CCEMG round due to its lower launch velocity of 1350 m/s. For the same level of terminal performance, the CCEMG round extends the range by roughly 3,000 m compared to the conventional round.

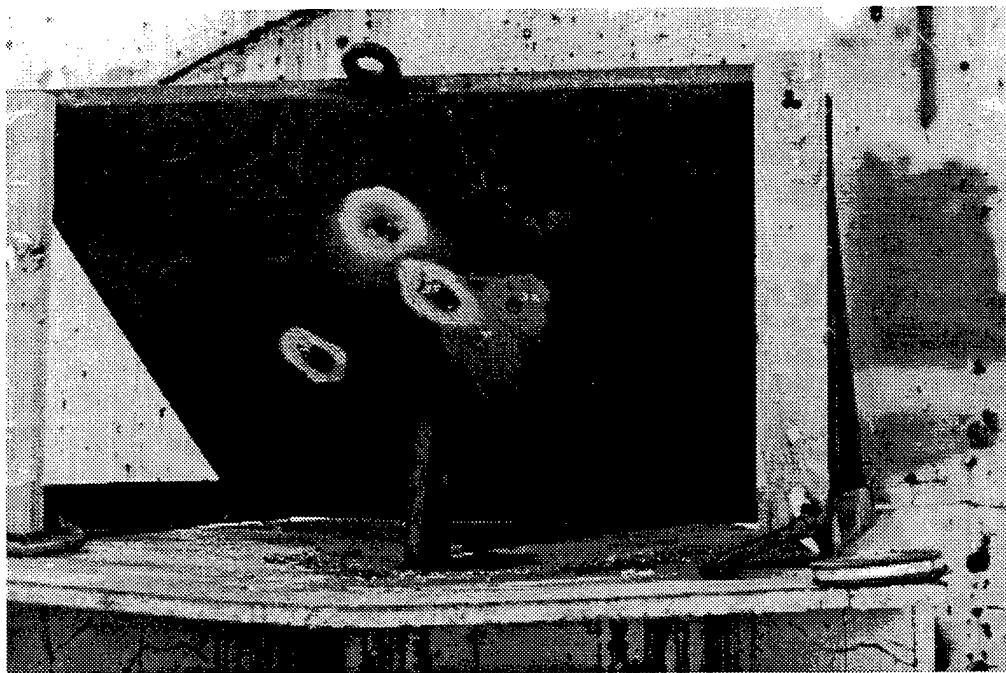


Figure 32. Front view of armor target and five subprojectile impacts.

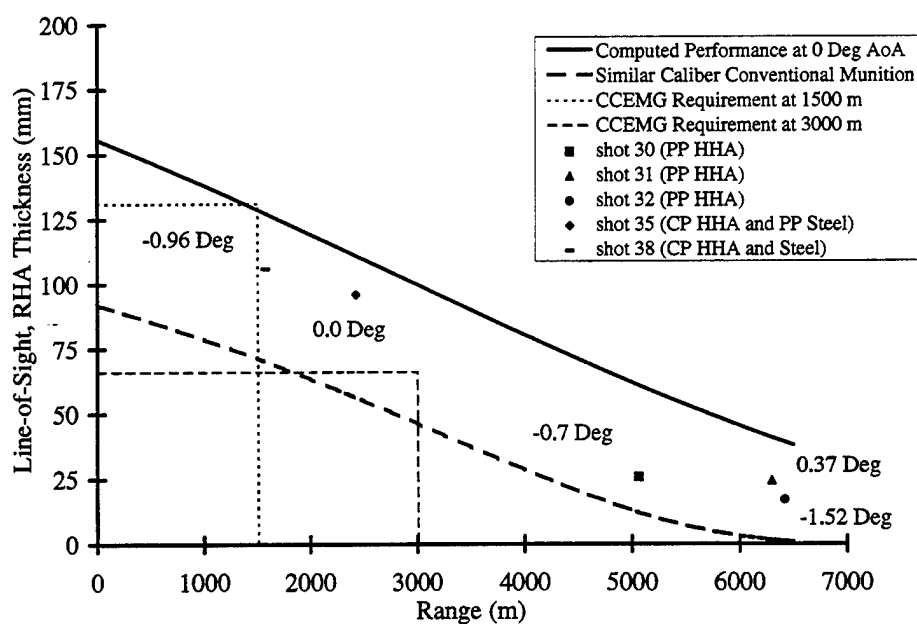


Figure 33. Terminal performance of the ILP subprojectile as a function of effective range.

7. Summary

The results presented in this report document the first comprehensive evaluation of launch and flight performance of an EM gun launched tactical projectile. Experimental techniques developed for conventional propellant gun systems have been adapted to quantify the launch disturbances of the current EM gun system and their effects on terminal accuracy and dispersion. Despite initial concerns regarding the potentially devastating effects of arcing at the muzzle, ILP and barrel-curvature interaction, and armature contact transition, the round was successfully fired through the range on each of the 39 shots performed as part of the current program. This effort represents the only U.S. electric gun program to launch, fly, and impact a tactical projectile configuration on a realistic target at a range appropriate for a cannon-caliber munition.

The importance of testing as part of the design cycle was demonstrated during the CCEMG program. For example, the quality of the armature discard and flight dynamics was vastly improved by jointly redesigning the ILP with Kaman Science Corporation during testing. It is doubtful that the initial design (i.e., the six-fin subprojectile and the baseline armature) would have survived high-current operation. Only through continued testing was it possible to rapidly turn design modifications into fully functional hardware.

The capacitor-based pulsed power supply was improved upon throughout the duration of the test program. At the initiation of testing the pulsed power supply had a energy capacity of 800 kJ. At the completion of testing the maximum energy capacity was 1.6 MJ and was operated at 91% of the maximum charge voltage. Furthermore, the muzzle switch, comprised of electronics, explosives, and hardware, was successfully incorporated to allow high-current operation of the launcher and ILP.

The results presented in this report indicate potential for a medium-caliber EM weapon system. The ILP has been launched at 96% of its design velocity and 86% of its design peak axial acceleration. Instrumentation, including radar, orthogonal multistation flash x-ray, smear and high-speed cameras, and yaw cards, was incorporated as part of the test matrix. The data from this equipment proved essential in diagnosing the ILP behavior.

Limited but sufficient data was acquired for each shot group to determine the relative contributions for the components of the jump survey, namely CG, SD, and AJ. The jump component dispersions and target impact dispersions are larger in the vertical direction than in the horizontal direction. The target impact dispersion was found to increase with velocity at a rate of roughly 1.4 mils/km/s. The AJ components of jump were also found to increase with velocity at nearly the same rate. The target impact dispersion for the CCEMG ILP at a similar caliber conventional launch velocity is estimated to be 1.3 mils in azimuth and 2.3 mils in elevation. Conventional rounds have much lower dispersion, albeit with considerably more time allocated to testing and development.

The results from the jump survey indicate that the individual component dispersions can be reduced with further engineering. For example, the aerodynamic jump can be decreased by judiciously increasing the fin area. Some portion of the sabot discard disturbance can be minimized through quality control of the ILP tolerances.

Maximum free-flight angular rates are less than $2.5^\circ/\text{m}$, with an average for all the shots of $1.2^\circ/\text{m}$. These rates are comparable to rates generated by similar caliber conventional launchers. Sabot discard disturbance is the significant contributor to the maximum free-flight angular rates. On average, more than half the rate due to sabot discard disturbance is located in the vertical direction.

In the vertical direction, the CG and AJ jump components each contribute roughly 40% towards the target impact dispersion. In the horizontal direction the SD component is the dominant contributor at 70% while the component due to aerodynamic jump is the smallest and contributes less than 10% to the total dispersion. It is believed that the forces that cause the linear and angular disturbances originate in the direction of sabot separation. The electrostatics associated with launcher disengagement can be a potential source affecting the sabot discard process. Inefficient aerodynamic features also contribute. Minimizing the disturbance and the duration of the interaction between the subprojectile and the armature should lead to decreased jump and dispersion.

Unlike acceleration in a conventional gun, the CCEMG sabot petal is not in a constant state compression in the horizontal direction (i.e., insulator plane). In a solid armature railgun, the bore insulators provide a guide for the ILP. This offers an explanation for the lower bias and dispersion observed in the horizontal plane for the CG jump component. There may also exist significant cross correlations between the jump components. However, the quantity of the x-ray data was insufficient to determine the interactions between the jump components.

CCEMG is designed to operate in a multishot mode. The test results discussed in this report cover single-shot operation. Remaining issues to be addressed include tests with the launcher in a recoil mount and a liquid-cooled multishot launcher. It is expected that the pointing angle (PA) and crossing velocity (CV) contributions to the CG jump will not be negligible.

INTENTIONALLY LEFT BLANK.

8. References

1. Kitzmiller, J. R., S. B. Pratap, M. D. Werst, C. E. Penney, T. J. Hotz, and B. T. Murphy. "Laboratory Testing of the Pulse Power System for the Cannon Caliber Electromagnetic Gun System (CCEMG)." *IEEE Trans. Magn.*, vol. 33, no. 1, pp. 443-448, January 1997.
2. Zielinski, A. E., and M. D. Werst. "Cannon-Caliber Electromagnetic Launcher." *IEEE Trans. Magn.*, vol. 33, no. 1, pp. 630-635, January 1997.
3. Zielinski, A. E., and D. Hildenbrand. "Observation and Simulation of Armature Contact Performance in the Cannon-Caliber Electromagnetic Gun." *IEEE Trans. Magn.*, vol. 33, no. 1, pp. 157-162, January 1997.
4. Hayden, T. E., R. Dethlefsen, and J. H. Price. "Effective Launch Package Integration for Electromagnetic Guns." *IEEE Trans. Magn.*, vol. 31, no. 1, pp. 150-155, January 1995.
5. Grover, F. W. *Inductance Calculations, Working Formulas and Tables*. New York: D. Van Nostrand, 1946.
6. Price, J. H., H. D. Yun, J. P. Kajs, J. R. Kitzmiller, S. B. Pratap, and M. D. Werst. "Discarding Armature and Barrel Optimization for a Cannon Caliber Electromagnetic Launcher System." *IEEE Trans. Magn.*, vol. 31, no. 1, pp. 225-230, January 1995.
7. Zielinski, A. E. "A Projectile-Oriented Design Study for a Cannon-Caliber Electromagnetic Launcher." *IEEE Trans. Magn.*, vol. 29, no. 1, pp. 889-894, January 1993.
8. Zielinski, A. E. "Preliminary Assessment of Recoil in a 15 mm Solid Armature Railgun." *Proceedings of the 11th Electromagnetic Launcher Association Meeting*, Huntington, WV, September 1993.
9. Kitzmiller, J. R., S. B. Pratap, T. A. Aanstoos, K. G. Cook, R. A. Kuenast, B. T. Murphy, and D. E. Perkins. "Optimization and Critical Design Issues of the Air Core Compulsator for the Cannon-Caliber Electromagnetic Launcher System (CCEML)." *IEEE Trans. Magn.*, vol. 31, no. 1, January 1995, pp. 61-66.
10. Werst, M. D., J. R. Kitzmiller, and A. E. Zielinski. "Rapid Fire Railgun for the Cannon Caliber Electromagnetic Gun System." *Proceedings of the 10th IEEE International Pulsed Power Conference*, Albuquerque, NM, July 1995.
11. Bornstein, J., I. Celmins, P. Plostins, and E. M. Schmidt. "Techniques for the Measurement of Tank Cannon Jump." BRL-MR-3715, U.S. Army Ballistic Research Laboratory, Aberdeen Proving Ground, MD, December 1988.
12. Murphy, C. H. "Free Flight Motion of Symmetric Missiles." Report No. 1216, U.S. Army Ballistic Research Laboratory, Aberdeen Proving Ground, MD, July 1963.
13. Schiff, L. B., and J. L. Steger. "Numerical Simulation of Steady Supersonic Viscous Flow." *AIAA Journal*, vol. 18, no. 12, pp. 1421-1430, December 1980.
14. Sturek, W. B., D. C. Mylin, B. J. Guidos, and C. J. Nietubicz. "Navier-Stokes Computational Study of the Influence of Shell Geometry on the Magnus Effect at Supersonic Speeds." BRL-TR-2501, U.S. Army Ballistic Research Laboratory, Aberdeen Proving Ground, MD, June 1983.

15. Weinacht, P., B. J. Guidos, L. D. Kayser, and W. B. Sturek. "PNS Computations for Spinning and Fin-Stabilized Projectiles at Supersonic Velocities." BRL-MR-3464, U.S. Army Ballistic Research Laboratory, Aberdeen Proving Ground, MD, September 1985.
16. Danberg, J. E., A. Sigal, and I. Celmins. "Prediction and Comparison with Measurements of the Aerodynamic Characteristics of Flare-Stabilized XM910 Prototypes." BRL-MR-3752, U.S. Army Ballistic Research Laboratory, Aberdeen Proving Ground, MD, May 1989.
17. Weinacht, P., and W. B. Sturek. "Navier-Stokes Predictions of Pitch Damping for Finned Projectiles Using Steady Coning Motion." AIAA Paper AIAA-90-3088, *Proceeding of the AIAA 8th Applied Aerodynamics Conference*, AIAA-CP 907, vol. 2, pp. 632-642, Portland, OR, August 1990.
18. Weinacht, P., W. B. Sturek, and L. B. Schiff. "Navier-Stokes Predictions of Pitch Damping for Axisymmetric Shell Using Steady Coning Motion." AIAA Paper AIAA-91-2855, *Proceeding of the AIAA 1991 Flight Mechanics Conference*, AIAA-CP 916, pp. 89-100, New Orleans, LA, August 1991.
19. Weinacht, P. "Navier-Stokes Predictions of Pitch Damping for a Family of Flared Projectiles." AIAA Paper AIAA-91-3339, *Proceedings of the AIAA 9th Applied Aerodynamics Conference*, AIAA-CP 918, vol. 2, pp. 1025-1034, Baltimore, MD, September 1991.
20. Weibel Scientific Corp. *Doppler Analyzer User's Guide, W-680*. Grusbakken 1-3, 2820 Gentofte, Denmark.
21. Plostins, P., K. P. Soencksen, A. E. Zielinski, and T. Hayden. "Aeroballistics Evaluation of Kinetic Energy Penetrators for Electromagnetic Gun Applications." AIAA 96-0454, presented at the 34th Aerospace Sciences Meeting and Exhibit, Reno, NV, January 1996.
22. Weinacht, P., and W. B. Sturek. "Navier-Stokes Predictions of Static and Dynamic Aerodynamic Derivatives for High L/D Finned Projectiles." AGARD Conf. Proc., AGARD-CP-493, Paper 20, April 1990.
23. Plostins, P., I. Celmins, and J. Bornstein. "The Effect of Sabot Borerider Stiffness on the Launch Dynamics of Fin-Stabilized Kinetic Energy Ammunition." AIAA-90-0066, presented at the 28th Aerospace Sciences Meeting, Reno, NV, January 1990.
24. Rapacki, E. J., K. Frank, R. B. Leavy, M. J. Keele, and J. J. Prifti. "Armor Steel Hardness Influence on Kinetic Energy Penetration." *Proceedings of the 15th International Symposium on Ballistics*, vol. 1, pp. 323-330, Jerusalem, Israel, May 1995.

NO. OF
COPIES ORGANIZATION

2 DEFENSE TECHNICAL
INFORMATION CENTER
DTIC DDA
8725 JOHN J KINGMAN RD
STE 0944
FT BELVOIR VA 22060-6218

1 HQDA
DAMO FDQ
DENNIS SCHMIDT
400 ARMY PENTAGON
WASHINGTON DC 20310-0460

1 CECOM
SP & TRRSTRL COMMCTN DIV
AMSEL RD ST MC M
H SOICHER
FT MONMOUTH NJ 07703-5203

1 PRIN DPTY FOR TCHNLGY HQ
US ARMY MATCOM
AMCDCG T
M FISETTE
5001 EISENHOWER AVE
ALEXANDRIA VA 22333-0001

1 PRIN DPTY FOR ACQUSTN HQS
US ARMY MATCOM
AMCDCG A
D ADAMS
5001 EISENHOWER AVE
ALEXANDRIA VA 22333-0001

1 DPTY CG FOR RDE HQS
US ARMY MATCOM
AMCRD
BG BEAUCHAMP
5001 EISENHOWER AVE
ALEXANDRIA VA 22333-0001

1 ASST DPTY CG FOR RDE HQS
US ARMY MATCOM
AMCRD
COL S MANESS
5001 EISENHOWER AVE
ALEXANDRIA VA 22333-0001

NO. OF
COPIES ORGANIZATION

1 DPTY ASSIST SCY FOR R&T
SARD TT F MILTON
THE PENTAGON RM 3E479
WASHINGTON DC 20310-0103

1 DPTY ASSIST SCY FOR R&T
SARD TT D CHAIT
THE PENTAGON
WASHINGTON DC 20310-0103

1 DPTY ASSIST SCY FOR R&T
SARD TT K KOMINOS
THE PENTAGON
WASHINGTON DC 20310-0103

1 DPTY ASSIST SCY FOR R&T
SARD TT B REISMAN
THE PENTAGON
WASHINGTON DC 20310-0103

1 DPTY ASSIST SCY FOR R&T
SARD TT T KILLION
THE PENTAGON
WASHINGTON DC 20310-0103

1 OSD
OUSD(A&T)/ODDDR&E(R)
J LUPO
THE PENTAGON
WASHINGTON DC 20301-7100

1 INST FOR ADVNCD TCHNLGY
THE UNIV OF TEXAS AT AUSTIN
PO BOX 202797
AUSTIN TX 78720-2797

1 DUSD SPACE
1E765 J G MCNEFF
3900 DEFENSE PENTAGON
WASHINGTON DC 20301-3900

1 USAASA
MOAS AI W PARRON
9325 GUNSTON RD STE N319
FT BELVOIR VA 22060-5582

NO. OF
COPIES ORGANIZATION

1 CECOM
PM GPS COL S YOUNG
FT MONMOUTH NJ 07703

1 GPS JOINT PROG OFC DIR
COL J CLAY
2435 VELA WAY STE 1613
LOS ANGELES AFB CA 90245-5500

1 ELECTRONIC SYS DIV DIR
CECOM RDEC
J NIEMELA
FT MONMOUTH NJ 07703

3 DARPA
L STOTTS
J PENNELLA
B KASPAR
3701 N FAIRFAX DR
ARLINGTON VA 22203-1714

1 SPCL ASST TO WING CMNDR
50SW/CCX
CAPT P H BERNSTEIN
300 O'MALLEY AVE STE 20
FALCON AFB CO 80912-3020

1 USAF SMC/CED
DMA/JPO
M ISON
2435 VELA WAY STE 1613
LOS ANGELES AFB CA 90245-5500

1 US MILITARY ACADEMY
MATH SCI CTR OF EXCELLENCE
DEPT OF MATHEMATICAL SCI
MDN A MAJ DON ENGEN
THAYER HALL
WEST POINT NY 10996-1786

1 DIRECTOR
US ARMY RESEARCH LAB
AMSRL CS AL TP
2800 POWDER MILL RD
ADELPHI MD 20783-1145

NO. OF
COPIES ORGANIZATION

1 DIRECTOR
US ARMY RESEARCH LAB
AMSRL CS AL TA
2800 POWDER MILL RD
ADELPHI MD 20783-1145

3 DIRECTOR
US ARMY RESEARCH LAB
AMSRL CI LL
2800 POWDER MILL RD
ADELPHI MD 20783-1145

ABERDEEN PROVING GROUND

2 DIR USARL
AMSRL CI LP (305)

NO. OF
COPIES ORGANIZATION

1 DIR FOR THE DIRECTORATE
OF FORCE DEVELOPMENT
US ARMY ARMOR CENTER
COL E BRYLA
FT KNOX KY 40121-5000

1 DPTY ASST SEC FOR RD&A
R CHAIT
THE PENTAGON RM 3E480
WASHINGTON DC 20310-0103

1 US ARMY MISSILE COMMAND
AMSMI RD
DR MCCORKLE
REDSTONE ARSENAL AL
35898-5240

3 CG MCRDAC
CODE AWT
ATTN DR C VAUGHN
G SOLHAND
MAJ F WYSOCKI
QUANTICO VA 22134-5080

1 US ARMY TACOM TARDEC
M TOURNER
AMSTA TR D MS #207
WARREN MI 48397-5000

3 US ARMY ARDEC
J BENNETT
AMSTA FSP E BLDG 382
PICATINNY ARSENAL NJ
07806-5000

2 US ARMY ARDEC
ATTN AMSTA AR CCL FA
H MOORE
B SCHLENNER
BLDG 65N
PICATINNY ARSENAL NJ
07806-5000

NO. OF
COPIES ORGANIZATION

3 INST FOR ADVANCED
TECH
UNIV OF TEXAS AT AUSTIN
P SULLIVAN
I MCNAB
J PARKER
4030-2 WEST BRAKER LANE
AUSTIN TX 78759-5329

1 KAMAN SCIENCES CORP
T HAYDEN
P O BOX 7463
COLORADO SPRINGS CO
80933

3 UNIV OF TEXAS AT AUSTIN
CENTER FOR ELECT
R ZOWARKA JR
J KITZMILLER
M WERST
PRC MAIL CODE R7000
AUSTIN TX 78712

1 LORAL VOUGHT SYS CORP
R J TAYLOR
MS WT-21
P O BOX 650003
DALLAS TX 75265-0003

1 INST FOR DEFENSE
ANALYSIS
I KOHLBERG
1801 N BEAUREGARD ST
ALEXANDRIA VA 22311

1 UNIV AT BUFFALO
SUNY/AB
J SARJEANT
P O BOX 601900
BUFFALO NY 14260-1900

2 UDLP
B GOODELL
MAIL STOP M170
4800 EAST RIVER ROAD
MINNEAPOLIS MN
55421-1498

NO. OF
COPIES ORGANIZATION

NO. OF
COPIES ORGANIZATION

1 UNIV OF TEXAS AT AUSTIN
M DRIGA
ENS 434 DEPT OF ECE
MAIL CODE 60803
AUSTIN TX 78712

1 SAJC
G CHRYSSOMALLIS
3800 WEST 80TH ST
SUITE 1090
BLOOMINGTON MN
55431

1 SAJC
J BATTEH
1225 JOHNSON FERRY RD
SUITE 100
MARIETTA GA 30068

1 SAJC
K A JAMISON
1247 B N EGLIN PKWY
SHALIMAR FL 32579

2 IAP RESEARCH INC
J P BARBER
D BAUER
2763 CULVER AVE
DAYTON OH 45429-3723

2 MAXWELL LAB
F LEVINE
T R WOLFE
9244 BALBOA AVE
SAN DIEGO CA 92123

ABERDEEN PROVING GROUNDS

41 DIR USARL
ATTN AMSRL WM
I MAY
L JOHNSON
D ECCLESHALL
AMSRL WM P
A HORST
E SCHMIDT
AMSRL WM WD
J POWELL

AMSRL WM PA
G KELLER
AMSRL WM PC
B FORCH
AMSRL WM PD
B BURNS

AMSRL WM PA
T MINOR
G KATULKA
G WREN
J DESPIRITO
A JUHASZ

C LEVERITT
M MCQUAID
W OBERLE
P TRAN
K WHITE

J COLBURN
P CONROY
D KOOKER

M NUSCA
T ROSENBERGER

AMSRL WM PB
P PLOSTINS
D LYON

J GARNER
V OSKAY

M BUNDY
J SAHU

P WEINACHT
H EDGE

B GUIDOS
E FERRY

Z ZIELINSKI
D WEBB

K SOENCKSEN

AMSRL WM PD
J NEWILL

D HOPKINS

AMSRL CI H

W STUREK

C NIETUBICZ

REPORT DOCUMENTATION PAGE			Form Approved OMB No. 0704-0188	
Public reporting burden for this collection of information is estimated to average 1 hour per response, including the time for reviewing instructions, searching existing data sources, gathering and maintaining the data needed, and completing and reviewing the collection of information. Send comments regarding this burden estimate or any other aspect of this collection of information, including suggestions for reducing this burden, to Washington Headquarters Services, Directorate for Information Operations and Reports, 1215 Jefferson Davis Highway, Suite 1204, Arlington, VA 22202-4302, and to the Office of Management and Budget, Paperwork Reduction Project (0704-0188), Washington, DC 20503.				
1. AGENCY USE ONLY (Leave blank)	2. REPORT DATE June 1997	3. REPORT TYPE AND DATES COVERED Final, August 1994 - March 1997		
4. TITLE AND SUBTITLE An Investigation of the Ballistic Performance for an Electromagnetic Gun-Launched Projectile		5. FUNDING NUMBERS PR: 1L162618AH80		
6. AUTHOR(S) Alexander E. Zielinski, Paul Weinacht, David W. Webb, and Keith P. Soencksen				
7. PERFORMING ORGANIZATION NAME(S) AND ADDRESS(ES) U.S. Army Research Laboratory ATTN: AMSRL-WM-PB Aberdeen Proving Ground, MD 21005-5066		8. PERFORMING ORGANIZATION REPORT NUMBER ARL-TR-1361		
9. SPONSORING/MONITORING AGENCY NAME(S) AND ADDRESS(ES)		10. SPONSORING/MONITORING AGENCY REPORT NUMBER		
11. SUPPLEMENTARY NOTES				
12a. DISTRIBUTION/AVAILABILITY STATEMENT Approved for public release; distribution is unlimited.		12b. DISTRIBUTION CODE		
13. ABSTRACT (Maximum 200 words) The Cannon-Caliber Electromagnetic Gun (CCEMG) Program is a major effort toward proving the viability of electromagnetic (EM) weapons for future use by the armed services. Crucial to the success of the program are the operational characteristics of the launcher and the integrated launch package (ILP), which consists of an armature/sabot and a subprojectile. To date, 39 shots have been fired at the U.S. Army Research Laboratory (ARL) using a 1.6-MJ capacitor bank and CCEMG Launcher IIa. Free-flight aerodynamic data indicated that the subprojectile has adequate in-flight stability. An analysis of the transitional ballistic process has been performed to quantify the contributors to the total launch disturbance. The jump component dispersion and target impact dispersion are larger in the vertical direction than in the horizontal direction. In the vertical direction, the center of gravity and aerodynamic jump contributions are dominant and roughly equal. In the horizontal direction, the sabot discard is the dominant jump component. Round-to-round dispersion was computed over a wide range of launch velocities based on downrange impact locations. Impact data on armor were limited, but nonetheless indicated that the round is capable of meeting the CCEMG system requirements. The results presented here represent the first known experimental assessment of these parameters obtained from EM railgun firings.				
14. SUBJECT TERMS EM guns, accuracy, jump, aerodynamics, pulsed power, dispersion, medium-caliber		15. NUMBER OF PAGES 57		
		16. PRICE CODE		
17. SECURITY CLASSIFICATION OF REPORT UNCLASSIFIED	18. SECURITY CLASSIFICATION OF THIS PAGE UNCLASSIFIED	19. SECURITY CLASSIFICATION OF ABSTRACT UNCLASSIFIED	20. LIMITATION OF ABSTRACT SAR	

INTENTIONALLY LEFT BLANK.

USER EVALUATION SHEET/CHANGE OF ADDRESS

This Laboratory undertakes a continuing effort to improve the quality of the reports it publishes. Your comments/answers to the items/questions below will aid us in our efforts.

1. ARL Report Number/Author ARL-TR-1361 (Zielinski) Date of Report June 1997
2. Date Report Received _____
3. Does this report satisfy a need? (Comment on purpose, related project, or other area of interest for which the report will be used.) _____

4. Specifically, how is the report being used? (Information source, design data, procedure, source of ideas, etc.) _____

5. Has the information in this report led to any quantitative savings as far as man-hours or dollars saved, operating costs avoided, or efficiencies achieved, etc? If so, please elaborate. _____

6. General Comments. What do you think should be changed to improve future reports? (Indicate changes to organization, technical content, format, etc.) _____

CURRENT
ADDRESS

Organization

Name

E-mail Name

Street or P.O. Box No.

City, State, Zip Code

7. If indicating a Change of Address or Address Correction, please provide the Current or Correct address above and the Old or Incorrect address below.

OLD
ADDRESS

Organization

Name

Street or P.O. Box No.

City, State, Zip Code

(Remove this sheet, fold as indicated, tape closed, and mail.)
(DO NOT STAPLE)

DEPARTMENT OF THE ARMY

OFFICIAL BUSINESS

BUSINESS REPLY MAIL
FIRST CLASS PERMIT NO 0001,APG,MD

POSTAGE WILL BE PAID BY ADDRESSEE

DIRECTOR
US ARMY RESEARCH LABORATORY
ATTN AMSRL WM PB
ABERDEEN PROVING GROUND MD 21005-5066



NO POSTAGE
NECESSARY
IF MAILED
IN THE
UNITED STATES

